



OPEN ACCESS

EDITED BY

You-wei Wen,
Hunan Normal University, China

REVIEWED BY

Saneera Hemantha Kulathilake,
Rajarata University of Sri Lanka, Sri Lanka
Yide Zhang,
California Institute of Technology, United States
Tingting Wu,
Nanjing University of Posts and
Telecommunications, China

*CORRESPONDENCE

Kevin Bui
✉ kevinb3@uci.edu

RECEIVED 24 December 2022

ACCEPTED 03 May 2023

PUBLISHED 28 June 2023

CITATION

Bui K, Lou Y, Park F and Xin J (2023) Difference of anisotropic and isotropic TV for segmentation under blur and Poisson noise. *Front. Comput. Sci.* 5:1131317.
doi: 10.3389/fcomp.2023.1131317

COPYRIGHT

© 2023 Bui, Lou, Park and Xin. This is an open-access article distributed under the terms of the [Creative Commons Attribution License \(CC BY\)](#). The use, distribution or reproduction in other forums is permitted, provided the original author(s) and the copyright owner(s) are credited and that the original publication in this journal is cited, in accordance with accepted academic practice. No use, distribution or reproduction is permitted which does not comply with these terms.

Difference of anisotropic and isotropic TV for segmentation under blur and Poisson noise

Kevin Bui^{1*}, Yifei Lou², Fredrick Park³ and Jack Xin¹

¹Department of Mathematics, University of California, Irvine, Irvine, CA, United States, ²Department of Mathematical Sciences, University of Texas at Dallas, Richardson, TX, United States, ³Department of Mathematics & Computer Science, Whittier College, Whittier, CA, United States

In this paper, we aim to segment an image degraded by blur and Poisson noise. We adopt a smoothing-and-thresholding (SaT) segmentation framework that finds a piecewise-smooth solution, followed by k -means clustering to segment the image. Specifically for the image smoothing step, we replace the least-squares fidelity for Gaussian noise in the Mumford-Shah model with a maximum posterior (MAP) term to deal with Poisson noise and we incorporate the weighted difference of anisotropic and isotropic total variation (AITV) as a regularization to promote the sparsity of image gradients. For such a nonconvex model, we develop a specific splitting scheme and utilize a proximal operator to apply the alternating direction method of multipliers (ADMM). Convergence analysis is provided to validate the efficacy of the ADMM scheme. Numerical experiments on various segmentation scenarios (grayscale/color and multiphase) showcase that our proposed method outperforms a number of segmentation methods, including the original SaT.

KEYWORDS

image segmentation, total variation, nonconvex optimization, ADMM, Poisson noise

1. Introduction

Image segmentation partitions an image into multiple, coherent regions, where pixels of one region share similar characteristics such as colors, textures, and edges. It remains an important yet challenging problem in computer vision that has various applications, including magnetic resonance imaging (Duan et al., 2015; Tongbram et al., 2021; Li et al., 2022) and microscopy (Zosso et al., 2017; Bui et al., 2020). One of the most fundamental models for image segmentation is the Mumford-Shah model (Mumford and Shah, 1989) because of its robustness to noise. Given an input image $f: \Omega \rightarrow \mathbb{R}$ defined on an open, bounded, and connected domain $\Omega \subset \mathbb{R}^2$, the Mumford-Shah model is formulated as

$$\min_{u, \Gamma} E_{MS}(u, \Gamma) := \frac{\lambda}{2} \int_{\Omega} (f - u)^2 \, dx + \frac{\mu}{2} \int_{\Omega \setminus \Gamma} |\nabla u|^2 \, dx + \text{Length}(\Gamma), \quad (1)$$

where $u: \Omega \rightarrow \mathbb{R}$ is a piecewise-smooth approximation of the image f , $\Gamma \subset \Omega$ is a compact curve representing the region boundaries, and $\lambda, \mu > 0$ are the weight parameters. The first term in (1) is the fidelity term that ensures that the solution u approximates the image f . The second term enforces u to be piecewise smooth on $\Omega \setminus \Gamma$. The last term measures the perimeter, or more mathematically the one-dimensional Haussdorf measure in \mathbb{R}^2 (Bar et al., 2011), of the curve Γ . However, (1) is difficult to solve because the unknown set of boundaries needs to be discretized. One common approach involves approximating the objective function in (1) by a sequence of elliptic functionals (Ambrosio and Tortorelli, 1990).

Alternatively, [Chan and Vese \(2001\)](#) (CV) simplified (1) by assuming the solution u to be piecewise constant with two phases or regions, thereby making the model easier to solve via the level-set method ([Osher and Sethian, 1988](#)). Let the level-set function ϕ be Lipschitz continuous and be defined as follows:

$$\begin{cases} \phi(x) > 0 & \text{if } x \text{ is inside } \Gamma, \\ \phi(x) = 0 & \text{if } x \text{ is at } \Gamma, \\ \phi(x) < 0 & \text{if } x \text{ is outside } \Gamma. \end{cases}$$

By the definition of ϕ , the curve Γ is represented by $\phi(x) = 0$. The image region can be defined as either inside or outside the curve Γ . In short, the CV model is formulated as

$$\begin{aligned} \min_{c_1, c_2, \phi} E_{CV}(c_1, c_2, \phi) := & \lambda \left(\int_{\Omega} |f - c_1|^2 H(\phi) dx \right. \\ & + \int_{\Omega} |f - c_2|^2 (1 - H(\phi)) dx \Big) \\ & + \nu \int_{\Omega} |\nabla H(\phi)| dx, \end{aligned} \quad (2)$$

where λ, ν are weight parameters, the constants c_1, c_2 are the mean intensity values of the two regions, and $H(\phi)$ is the Heaviside function defined by $H(\phi) = 1$ if $\phi \geq 0$ and $H(\phi) = 0$ otherwise. A convex relaxation ([Chan et al., 2006](#)) of (2) was formulated as

$$\begin{aligned} \min_{c_1, c_2, u \in [0,1]} \lambda \left(\int_{\Omega} |f - c_1|^2 u dx + \int_{\Omega} |f - c_2|^2 (1 - u) dx \right) \\ + \nu \int_{\Omega} |\nabla u| dx, \end{aligned}$$

where an image segmentation \tilde{u} is obtained by thresholding u , that is

$$\tilde{u}(x) = \begin{cases} 1 & \text{if } u(x) > \tau, \\ 0 & \text{if } u(x) \leq \tau, \end{cases}$$

for some value $\tau \in (0, 1)$. It can be solved efficiently by convex optimization algorithms, such as the alternating direction method of multipliers (ADMM) ([Boyd et al., 2011](#)) and primal-dual hybrid gradient ([Chambolle and Pock, 2011](#)). A multiphase extension of (2) was proposed in [Vese and Chan \(2002\)](#), but it requires that the number of regions to be segmented is a power of 2. For segmenting into an arbitrary number of regions, fuzzy membership functions were incorporated ([Li et al., 2010](#)).

[Cai et al. \(2013\)](#) proposed the smoothing-and-thresholding (SaT) framework that is related to the model (1). In the smoothing step of SaT, a convex variant of (1) is formulated as

$$u^* = \arg \min_u \frac{\lambda}{2} \int_{\Omega} (f - Au)^2 dx + \frac{\mu}{2} \int_{\Omega} |\nabla u|^2 dx + \int_{\Omega} |\nabla u| dx, \quad (3)$$

yielding a piecewise-smooth solution u^* . The blurring operator A is included in the case when the image f is blurred. The total variation (TV) term $\int_{\Omega} |\nabla u| dx$ is a convex approximation of the length term in (2) by the coarea formula ([Chan et al., 2006](#)). After the smoothing step, a thresholding step is applied to the smooth image u^* to segment it into multiple regions. The two-stage framework

has many advantages. First, the smoothing model (3) is strongly convex, so it can be solved by any convex optimization algorithm to obtain a unique solution u^* . Second, the user can adjust the number of thresholds to segment u^* and the threshold values to obtain a satisfactory segmentation result, thanks to the flexibility of the thresholding step. Furthermore, the SaT framework can be adapted to color images by incorporating an intermediate lifting step ([Cai et al., 2017](#)). Before performing the thresholding step, the lifting step converts the RGB space to Lab (perceived lightness, red-green and yellow-blue) color space and concatenates both RGB and Lab intensity values into a six-channel image. The multi-stage framework for color image segmentation is called smoothing, lifting, and thresholding (SLaT).

One limitation of (3) lies in the ℓ_2 fidelity term that is statistically designed for images corrupted by additive Gaussian noise, and as a result, the smoothing step is not applicable to other types of noise distribution. In this paper, we aim at Poisson noise, which is commonly encountered when an image is taken by photon-capturing devices such as in positron emission tomography ([Vardi et al., 1985](#)) and astronomical imaging ([Lantéri and Theys, 2005](#)). By using the data fidelity term of $Au - f \log Au$ ([Le et al., 2007](#)), we obtain a smoothing model that is appropriate for Poisson noise ([Chan et al., 2014](#)):

$$\min_u \lambda \int_{\Omega} (Au - f \log Au) dx + \frac{\mu}{2} \int_{\Omega} |\nabla u|^2 dx + \int_{\Omega} |\nabla u| dx. \quad (4)$$

As a convex approximation of the length term in (1), the TV term in (4) can be further improved by nonconvex regularizations. The TV regularization is defined by the ℓ_1 norm of the image gradient. Literature has shown that nonconvex regularizations often yield better performance than the convex ℓ_1 norm in identifying sparse solutions. Examples of nonconvex regularization include $\ell_p, 0 < p < 1$ ([Chartrand, 2007](#); [Xu Z. et al., 2012](#); [Cao et al., 2013](#)), $\ell_1 - \alpha \ell_2, \alpha \in [0, 1]$ ([Lou et al., 2015a,b](#); [Ding and Han, 2019](#); [Li P. et al., 2020](#); [Ge and Li, 2021](#)), ℓ_1/ℓ_2 ([Rahimi et al., 2019](#); [Wang et al., 2020](#); [Xu et al., 2021](#)), and an error function ([Guo et al., 2021](#)). [Lou et al. \(2015c\)](#) designed a TV version of $\ell_1 - \alpha \ell_2$ called the weighted difference of anisotropic-isotropic total variation (AITV), which outperforms TV in various imaging applications, such as image denoising ([Lou et al., 2015c](#)), image reconstruction ([Lou et al., 2015c](#); [Li P. et al., 2020](#)), and image segmentation ([Bui et al., 2021, 2022](#); [Wu et al., 2022b](#)).

In this paper, we propose an AITV variant of (4) to improve the smoothing step of the SaT/SLaT framework for images degraded by Poisson noise and/or blur. Incorporating AITV regularization is motivated by our previous works ([Park et al., 2016](#); [Bui et al., 2021, 2022](#)), where we demonstrated that AITV regularization is effective in preserving edges and details, especially under Gaussian and impulsive noise. To maintain similar computational efficiency as the original SaT/SLaT framework, we propose an ADMM algorithm that utilizes the $\ell_1 - \alpha \ell_2$ proximal operator ([Lou and Yan, 2018](#)). The main contributions of this paper are as follows:

- We propose an AITV-regularized variant of (4) and prove the existence of a minimizer for the model.
- We develop a computationally efficient ADMM algorithm and provide its convergence analysis under certain conditions.

- We conduct numerical experiments on various grayscale/color images to demonstrate the effectiveness of the proposed approach.

The rest of the paper is organized as follows. Section 2 describes the background information such as notations, Poisson noise, and the SaT/SLaT framework. In Section 3, we propose a simplified Mumford-Shah model with AITV and a MAP data fidelity term for Poisson noise. In the same section, we show that the model has a global minimizer and develop an ADMM algorithm with convergence analysis. In Section 4, we evaluate the performance of the AITV Poisson SaT/SLaT framework on various grayscale and color images. Lastly, we conclude the paper in Section 5.

2. Preliminaries

2.1. Notation

Throughout the rest of the paper, we represent images and mathematical models in discrete notations (i.e., vectors and matrices). An image is represented as an $M \times N$ matrix, and hence the image domain is denoted by $\Omega = \{1, 2, \dots, M\} \times \{1, 2, \dots, N\}$. We define two inner product spaces: $X := \mathbb{R}^{M \times N}$ and $Y := X \times X$. Let $u \in X$. For shorthand notation, we define $u \geq 0$ if $u_{i,j} \geq 0$ for all $(i, j) \in \Omega$. The discrete gradient operator $\nabla : X \rightarrow Y$ is defined by $(\nabla u)_{i,j} = [(\nabla_x u)_{i,j}, (\nabla_y u)_{i,j}]$, where

$$(\nabla_x u)_{i,j} = \begin{cases} u_{i,j} - u_{i,j-1} & \text{if } 2 \leq j \leq N, \\ u_{i,1} - u_{i,N} & \text{if } j = 1, \end{cases}$$

and

$$(\nabla_y u)_{i,j} = \begin{cases} u_{i,j} - u_{i-1,j} & \text{if } 2 \leq i \leq M, \\ u_{1,j} - u_{M,j} & \text{if } i = 1. \end{cases}$$

The space X is equipped with the standard inner product $\langle \cdot, \cdot \rangle_X$, and Euclidean norm $\|\cdot\|_2$. The space Y has the following inner product and norms: for $p = (p_1, p_2) \in Y$ and $q = (q_1, q_2) \in Y$,

$$\begin{aligned} \langle p, q \rangle_Y &= \langle p_1, q_1 \rangle_X + \langle p_2, q_2 \rangle_X, \\ \|p\|_1 &= \sum_{i=1}^M \sum_{j=1}^N |(p_1)_{i,j}| + |(p_2)_{i,j}|, \\ \|p\|_2 &= \sqrt{\sum_{i=1}^M \sum_{j=1}^N |(p_1)_{i,j}|^2 + |(p_2)_{i,j}|^2}, \\ \|p\|_{2,1} &= \sum_{i=1}^M \sum_{j=1}^N \sqrt{(p_1)_{i,j}^2 + (p_2)_{i,j}^2}. \end{aligned}$$

For brevity, we omit the subscript X or Y in the inner product when its context is clear.

2.2. AITV regularization

There are two popular discretizations of total variation: the isotropic TV (Rudin et al., 1992) and the anisotropic TV

(Choksi et al., 2011), which are defined by

$$\|\nabla u\|_{2,1} = \sum_{i=1}^M \sum_{j=1}^N \sqrt{|(\nabla_x u)_{i,j}|^2 + |(\nabla_y u)_{i,j}|^2},$$

$$\|\nabla u\|_1 = \sum_{i=1}^M \sum_{j=1}^N |(\nabla_x u)_{i,j}| + |(\nabla_y u)_{i,j}|,$$

respectively. This work is based on the weighted difference between anisotropic and isotropic TV (AITV) regularization (Lou et al., 2015c), defined by

$$\begin{aligned} \|\nabla u\|_1 - \alpha \|\nabla u\|_{2,1} &= \sum_{i=1}^M \sum_{j=1}^N \left(|(\nabla_x u)_{i,j}| + |(\nabla_y u)_{i,j}| \right. \\ &\quad \left. - \alpha \sqrt{|(\nabla_x u)_{i,j}|^2 + |(\nabla_y u)_{i,j}|^2} \right), \end{aligned} \quad (5)$$

for a weighting parameter $\alpha \in [0, 1]$. The range of α ensures the non-negativity of the AITV regularization. Note that anisotropic TV is defined as the ℓ_1 norm of the image gradient $[(\nabla_x u)_{i,j}, (\nabla_y u)_{i,j}]$ at the pixel location $(i, j) \in \Omega$, while isotropic TV is the ℓ_2 norm on the gradient vector. As a result, AITV can be viewed as the $\ell_1 - \alpha \ell_2$ regularization on the gradient vector at every pixel, thereby enforcing sparsity individually at each gradient vector.

2.3. Poisson noise

Poisson noise follows the Poisson distribution with mean and variance η , whose probability mass function is given by

$$\mathbb{P}_\eta(n) = \frac{e^{-\eta} \eta^n}{n!}, \quad n \geq 0. \quad (6)$$

For a clean image $g \in X$, its intensity value at each pixel $g_{i,j}$ serves as the mean and variance for the corresponding noisy observation $f \in X$ defined by

$$f_{i,j} \sim \text{Poisson}(g_{i,j}) \quad \forall (i, j) \in \Omega.$$

To recover the image g from the noisy image f , we find its maximum a posteriori (MAP) estimation u , which maximizes the probability $\mathbb{P}(u|f)$. By Bayes' theorem, we have

$$\mathbb{P}(u|f) = \frac{\mathbb{P}(f|u)\mathbb{P}(u)}{\mathbb{P}(f)}.$$

It further follows from the definition (6) that

$$\mathbb{P}(f_{i,j}|u_{i,j})\mathbb{P}(u_{i,j}) = \mathbb{P}_{u_{i,j}}(f_{i,j})\mathbb{P}(u_{i,j}) = \frac{e^{-u_{i,j}} u_{i,j}^{f_{i,j}}}{(f_{i,j})!} \mathbb{P}(u_{i,j}).$$

Since Poisson noise is i.i.d. pixelwise, we have

$$\mathbb{P}(u|f) = \prod_{(i,j) \in \Omega} \mathbb{P}(f_{i,j}|u_{i,j}) \frac{\mathbb{P}(u_{i,j})}{\mathbb{P}(f_{i,j})} = \prod_{(i,j) \in \Omega} \frac{e^{-u_{i,j}} u_{i,j}^{f_{i,j}}}{(f_{i,j})!} \frac{\mathbb{P}(u_{i,j})}{\mathbb{P}(f_{i,j})}.$$

The MAP estimate of $\mathbb{P}(u|f)$ is equivalent to its negative logarithm, thus leading to the following optimization problem:

$$\min_{u \geq 0} \sum_{(i,j) \in \Omega} u_{i,j} - f_{i,j} \log u_{i,j} - \log \mathbb{P}(u_{i,j}). \quad (7)$$

The last term $-\log \mathbb{P}(u_{i,j})$ can be regarded as an image prior or a regularization. For example, [Le et al. \(2007\)](#) considered the isotropic total variation as the image prior and proposed a Poisson denoising model

$$\min_{u \geq 0} \langle u - f \log u, \mathbb{1} \rangle + \|\nabla u\|_{2,1}, \quad (8)$$

where \log is applied pixelwise and $\mathbb{1}$ is the matrix whose entries are all 1's. The first term in (8) is a concise notation that is commonly used as a fidelity term for Poisson denoising in various imaging applications ([Le et al., 2007](#); [Chan et al., 2014](#); [Wen et al., 2016](#); [Chang et al., 2018](#); [Chowdhury et al., 2020a,b](#)).

2.4. Review of Poisson SaT/SLaT

A Poisson SaT framework ([Chan et al., 2014](#)) consists of two steps. Given a noisy grayscale image $f \in X$ corrupted by Poisson noise, the first step is the smoothing step that finds a piecewise-smooth solution u^* from the optimization model:

$$u^* = \arg \min_{u \geq 0} \lambda \langle Au - f \log Au, \mathbb{1} \rangle + \frac{\mu}{2} \|\nabla u\|_2^2 + \|\nabla u\|_{2,1}. \quad (9)$$

Then in the thresholding step, $K - 1$ threshold values $\tau_1 \leq \tau_2 \leq \dots \leq \tau_{K-1}$ are appropriately chosen to segment u^* into K regions, where the k th region is given by

$$\Omega_k = \{(i,j) \in \Omega : \tau_{k-1} \leq u_{i,j}^* < \tau_k\},$$

with $\tau_0 := \inf_{x \in \Omega} u^*(x)$. The thresholding step is typically performed by k -means clustering.

The Poisson smoothing, lifting, and thresholding (SLaT) framework ([Cai et al., 2017](#)) extends the Poisson SaT framework to color images. For a color image $f = (f_1, f_2, f_3) \in X \times X \times X$, the model (9) is applied to each color channel f_i for $i = 1, 2, 3$, thus leading to a smoothed color image $u^* = (u_1^*, u_2^*, u_3^*)$. An additional lifting step ([Luong, 1993](#)) is performed to transform u^* to (u'_1, u'_2, u'_3) in the Lab space (perceived lightness, red-green, and yellow-blue). The channels in Lab space are less correlated than in RGB space, so they may have useful information for segmentation. The RGB image and the Lab image are concatenated to form the multichannel image $\hat{u} := (u_1^*, u_2^*, u_3^*, u'_1, u'_2, u'_3)$, followed by the thresholding stage. Generally, k -means clustering yields K centroids c_1, \dots, c_K as constant vectors, which are used to form the region

$$\Omega_k = \left\{ (i,j) \in \Omega : \|\hat{u}_{i,j} - c_k\|_2 = \min_{1 \leq \kappa \leq K} \|\hat{u}_{i,j} - c_\kappa\|_2 \right\}$$

for $k = 1, \dots, K$ such that Ω_k 's are disjoint and $\bigcup_{k=1}^K \Omega_k = \Omega$.

```

1 Input:
    • image  $f = (f_1, \dots, f_d)$ 
    • blurring operator  $A$ 
    • fidelity parameter  $\lambda > 0$ 
    • smoothing parameter  $\mu \geq 0$ 
    • AITV parameter  $\alpha \in [0, 1]$ 
    • the number of regions in the image  $K$ 

2 Output: Segmentation  $\tilde{f}$ 
3 Stage one: Compute  $u_\ell$  by solving (11) separately
    for  $\ell = 1, \dots, d$ .
4 Stage two: if  $f$  is a grayscale image, i.e.,  $d = 1$  then
5   Go to stage three.
6 else if  $f$  is a color image, i.e.,  $d = 3$  then
7   transfer the solution  $u^* = (u_1^*, u_2^*, u_3^*)$  into Lab
    space to obtain  $(u'_1, u'_2, u'_3)$  and concatenate to
    form  $\hat{u} = (u_1^*, u_2^*, u_3^*, u'_1, u'_2, u'_3)$ .
8 Stage three: Apply  $k$ -means to obtain  $\{(c_k, \Omega_k)\}_{k=1}^K$ 
    and compute  $\tilde{f}$  by (10).

```

Algorithm 1. AITV Poisson SaT/SLaT.

After the thresholding step for both SaT/SLaT, we define a piecewise-constant approximation of the image f by

$$\tilde{f} = (\tilde{f}_1, \dots, \tilde{f}_d) \text{ such that } \tilde{f}_\ell = \sum_{k=1}^K c_{k,\ell} \mathbb{1}_{\Omega_k} \quad \forall \ell = 1, \dots, d, \quad (10)$$

where $c_{k,\ell}$ is the ℓ th entry of the constant vector c_k and

$$\mathbb{1}_{\Omega_k} = \begin{cases} 1 & \text{if } (i,j) \in \Omega_k, \\ 0 & \text{if } (i,j) \notin \Omega_k. \end{cases}$$

Recall that $d = 1$ when f is grayscale, and $d = 3$ when f is color.

3. Proposed approach

To improve the Poisson SaT/SLaT framework, we propose to replace the isotropic TV in (9) with AITV regularization. In other words, in the smoothing step, we obtain the smoothed image u^* from the optimization problem

$$\begin{aligned} u^* = \arg \min_u F(u) := & \lambda \langle Au - f \log Au, \mathbb{1} \rangle + \frac{\mu}{2} \|\nabla u\|_2^2 \\ & + \|\nabla u\|_1 - \alpha \|\nabla u\|_{2,1}, \end{aligned} \quad (11)$$

for $\alpha \in [0, 1]$. We establish that this model admits a global solution. We then develop an ADMM algorithm to find a solution and provide the convergence analysis. The overall segmentation approach is described in [Algorithm 1](#).

3.1. Model analysis

To establish the solution's existence of the proposed model (11), we start with Lemma 1, a discrete version of Poincaré's inequality

(Evans, 2010). In addition, we prove Lemma 2 and Proposition 3, leading to the global existence theorem (Theorem 4).

Lemma 1. There exists a constant $C > 0$ such that

$$\|u - \bar{u}\mathbb{1}\|_2 \leq C\|\nabla u\|_{2,1}, \quad (12)$$

for every $u \in X$ and $\bar{u} := \frac{1}{MN} \sum_{i=1}^M \sum_{j=1}^N u_{i,j}$.

Proof. We prove it by contradiction. Suppose there exists a sequence $\{u_k\}_{k=1}^{\infty}$ such that

$$\|u_k - \bar{u}_k\mathbb{1}\|_2 > k\|\nabla u_k\|_{2,1}, \quad (13)$$

where $\bar{u}_k = \frac{1}{MN} \sum_{i=1}^M \sum_{j=1}^N (u_k)_{i,j}$. For every k , we normalize each element in the sequence by $v_k = \frac{u_k - \bar{u}_k\mathbb{1}}{\|\bar{u}_k\mathbb{1}\|_2}$. It is straightforward that

$$\bar{v}_k = \frac{1}{MN} \sum_{i=1}^M \sum_{j=1}^N (v_k)_{i,j} = 0, \quad \|v_k\|_2 = 1 \quad \forall k \in \mathbb{N}. \quad (14)$$

By (13), we have

$$\|\nabla v_k\|_{2,1} < \frac{1}{k}. \quad (15)$$

As $\{v_k\}_{k=1}^{\infty}$ is bounded, there exists a convergent subsequence $\{v_{k_j}\}_{j=1}^{\infty}$ such that $v_{k_j} \rightarrow v^*$ for $v^* \in X$. It follows from (15) that $\|\nabla v^*\|_{2,1} = 0$. Since $\ker(\nabla) = \{c\mathbb{1} : c \in \mathbb{R}\}$, then v^* is a constant vector. However, (14) implies that $\bar{v}^* = 0$ and $\|v^*\|_2 = 1$. This contradiction proves the lemma. \square

Lemma 2. Suppose $\|f\|_{\infty} < \infty$ and $\min_{i,j} f_{i,j} > 0$. There exists a scalar $u_0 > 0$ such that we have $2(x - f_{i,j} \log x) \geq x$ for any $x \geq u_0$ and $(i,j) \in \Omega$.

Proof. For each $(i,j) \in \Omega$, we want to show that there exists $u_{i,j} > 0$ such that $H(x) := x - 2f_{i,j} \log x \geq 0$ for $x \geq u_{i,j}$. Since $H(x)$ is strictly convex and it attains a global minimum at $x = 2f_{i,j}$, it is increasing on the domain $x > 2f_{i,j}$. Additionally as x dominates $\log(x)$ as $x \rightarrow +\infty$, there exists $u_{i,j} > 2f_{i,j} > 0$ such that $\frac{u_{i,j}}{\log u_{i,j}} \geq 2f_{i,j}$, which implies that $H(u_{i,j}) = u_{i,j} - 2f_{i,j} \log u_{i,j} \geq 0$. As a result, for $x \geq u_{i,j} > 2f_{i,j}$, we obtain $x - 2f_{i,j} \log x = H(x) \geq H(u_{i,j}) \geq 0$. Define $u_0 := \max_{i,j} u_{i,j}$, and hence we have $2(x - f_{i,j} \log x) \geq x$ for $x \geq u_0 \geq u_{i,j}, \forall (i,j) \in \Omega$.

Proposition 3. Suppose $\ker(A) \cap \ker(\nabla) = \{0\}$ and $\{u_k\}_{k=1}^{\infty} \subset X$. If $\{(Au_k, \nabla u_k)\}_{k=1}^{\infty}$ is bounded, then $\{u_k\}_{k=1}^{\infty}$ is bounded.

Proof. Since $\ker(A) \cap \ker(\nabla) = \{0\}$, we have $A\mathbb{1} \neq 0$. Simple calculations lead to

$$\begin{aligned} |\bar{u}_k| \|A\mathbb{1}\|_2 &= \|A(\bar{u}_k\mathbb{1})\|_2 \leq \|A(\bar{u}_k\mathbb{1} - u_k)\|_2 + \|Au_k\|_2 \\ &\leq \|A\|\|u_k - \bar{u}_k\mathbb{1}\|_2 + \|Au_k\|_2 \\ &\leq C\|A\|\|\nabla u_k\|_{2,1} + \|Au_k\|_2, \end{aligned} \quad (16)$$

where the last inequality is due to Lemma 1. The boundedness of $\{Au_k\}_{k=1}^{\infty}$ and $\{\nabla u_k\}_{k=1}^{\infty}$ implies that $\{u_k\}_{k=1}^{\infty}$ is also bounded by (16). We apply Lemma 1 to obtain

$$\|u_k\|_2 \leq \|u_k - \bar{u}_k\mathbb{1}\|_2 + \|\bar{u}_k\mathbb{1}\|_2 < C\|\nabla u_k\|_{2,1} + \|\bar{u}_k\mathbb{1}\|_2 < \infty,$$

which thereby proves that $\{u_k\}_{k=1}^{\infty}$ is bounded.

Finally, we adapt the proof in Chan et al. (2014) to establish that F has a global minimizer.

Theorem 4. Suppose $\|f\|_{\infty} < \infty$ and $\min_{i,j} f_{i,j} > 0$. If $\lambda > 0, \mu \geq 0, \alpha \in [0, 1)$, and $\ker(A) \cap \ker(\nabla) = \{0\}$, then F has a global minimizer.

Proof. It is straightforward that $\|\nabla u\|_{2,1} \leq \|\nabla u\|_1$, thus $\|\nabla u\|_1 - \alpha\|\nabla u\|_{2,1} \geq 0$ for $\alpha \in [0, 1)$. As a result, we have

$$F(u) \geq \lambda \langle Au - f \log Au, \mathbb{1} \rangle = \lambda \sum_{i=1}^M \sum_{j=1}^N (Au)_{i,j} - f_{i,j} \log(Au)_{i,j}.$$

Given a scalar $f > 0$, the function $G(x) = x - f \log(x)$ attains its global minimum at $x = f$. Therefore, we have $x - f_{i,j} \log x \geq f_{i,j} - f_{i,j} \log f_{i,j}$ for all $x > 0$ and $(i,j) \in \Omega$, which leads to a lower bound of $F(u)$, i.e.,

$$\begin{aligned} F(u) &\geq \lambda \sum_{i=1}^M \sum_{j=1}^N (Au)_{i,j} - f_{i,j} \log(Au)_{i,j} \\ &\geq \lambda \sum_{i=1}^M \sum_{j=1}^N f_{i,j} - f_{i,j} \log f_{i,j} =: F_0. \end{aligned} \quad (17)$$

As $F(u)$ is lower bounded by F_0 , we can choose a minimizing sequence $\{u_k\}_{k=1}^{\infty}$ and hence $F(u_k)$ has a uniform upper bound, denoted by B_1 , i.e., $F(u_k) < B_1$ for all $k \in \mathbb{N}$. It further follows from (17) that

$$B_1 \geq F(u_k) \geq \lambda \langle Au_k - f \log Au_k, \mathbb{1} \rangle \geq F_0,$$

which implies that $\{|\langle Au_k - f \log Au_k, \mathbb{1} \rangle|\}_{k=1}^{\infty}$ is uniformly bounded, i.e., there exists a constant $B_2 > 0$ such that $|\langle Au_k - f \log Au_k, \mathbb{1} \rangle| < B_2, \forall k$. Using these uniform bounds, we derive that

$$\begin{aligned} (1 - \alpha)\|\nabla u_k\|_1 &\leq \frac{\mu}{2} \|\nabla u_k\|_2^2 + \|\nabla u_k\|_1 - \alpha\|\nabla u_k\|_{2,1} \\ &= F(u_k) - \lambda \langle Au_k - f \log Au_k, \mathbb{1} \rangle \leq B_1 + \lambda B_2. \end{aligned}$$

As $\alpha < 1$, the sequence $\{\nabla u_k\}_{k=1}^{\infty}$ is bounded.

To prove the boundedness of $\{Au_k\}_{k=1}^{\infty}$, we introduce the notations of $x^+ = \max(x, 0)$ and $x^- = -\min(x, 0)$ for any $x \in \mathbb{R}$.

Then $x = x^+ - x^-$. By Lemma 2, there exists $u_0 > 0$ such that $2(x - f_{i,j} \log x) \geq x$, $\forall x \geq u_0$ and $(i, j) \in \Omega$. We observe that

$$\begin{aligned} \|Au_k\|_1 &= \sum_{i=1}^M \sum_{j=1}^N |(Au_k)_{i,j}| \\ &\leq \sum_{i=1}^M \sum_{j=1}^N \max\{2((Au_k)_{i,j} - f_{i,j} \log(Au_k)_{i,j}), u_0\} \\ &\leq 2 \sum_{i=1}^M \sum_{j=1}^N ((Au_k)_{i,j} - f_{i,j} \log(Au_k)_{i,j})^+ + MNu_0 \\ &= 2 \sum_{i=1}^M \sum_{j=1}^N \left[((Au_k)_{i,j} - f_{i,j} \log(Au_k)_{i,j})^+ + ((Au_k)_{i,j} - f_{i,j} \log(Au_k)_{i,j})^- \right] + MNu_0 \\ &= 2 \langle Au_k - f \log Au_k, \mathbb{1} \rangle \\ &\quad + 2 \sum_{i=1}^M \sum_{j=1}^N ((Au_k)_{i,j} - f_{i,j} \log(Au_k)_{i,j})^- + MNu_0 \\ &\leq 2B_2 + 2 \sum_{i=1}^M \sum_{j=1}^N |f_{i,j} - f_{i,j} \log f_{i,j}| + MNu_0 < \infty. \end{aligned} \quad (18)$$

This shows that $\{Au_k\}_{k=1}^\infty$ is bounded.

Since both $\{\nabla u_k\}_{k=1}^\infty$ and $\{Au_k\}_{k=1}^\infty$ are bounded, then $\{u_k\}_{k=1}^\infty$ is bounded due to Proposition 3. Therefore, there exists a subsequence $\{u_{k_n}\}_{n=1}^\infty$ that converges to some $u^* \in X$. As F is continuous and thus lower semicontinuous, we have

$$F(u^*) \leq \liminf_{n \rightarrow \infty} F(u_{k_n}),$$

which means that u^* minimizes F .

3.2. Numerical algorithm

To minimize (11), we introduce two auxiliary variables $v \in X$ and $w = (w_x, w_y) \in Y$, leading to an equivalent constrained optimization problem:

$$\begin{aligned} \min_{u, v, w} \quad & \lambda \langle v - f \log v, \mathbb{1} \rangle + \frac{\mu}{2} \|\nabla u\|_2^2 + \|w\|_1 - \alpha \|w\|_{2,1} \\ \text{s.t.} \quad & Au = v, \quad \nabla u = w. \end{aligned} \quad (19)$$

The corresponding augmented Lagrangian is expressed as

$$\begin{aligned} \mathcal{L}_{\beta_1, \beta_2}(u, v, w, y, z) &= \lambda \langle v - f \log v, \mathbb{1} \rangle + \frac{\mu}{2} \|\nabla u\|_2^2 + \|w\|_1 - \alpha \|w\|_{2,1} \\ &\quad + \langle y, Au - v \rangle + \frac{\beta_1}{2} \|Au - v\|_2^2 + \langle z, \nabla u - w \rangle \\ &\quad + \frac{\beta_2}{2} \|\nabla u - w\|_2^2, \end{aligned} \quad (20)$$

where $y \in X$ and $z = (z_x, z_y) \in Y$ are Lagrange multipliers and β_1, β_2 are positive parameters. We then apply the alternating direction method of multipliers (ADMM) to minimize (19) that consists of the following steps per iteration k :

$$u_{k+1} = \arg \min_u \mathcal{L}_{\beta_1, \beta_2, k}(u, v_k, w_k, y_k, z_k), \quad (21a)$$

$$v_{k+1} = \arg \min_v \mathcal{L}_{\beta_1, \beta_2, k}(u_{k+1}, v, w_k, y_k, z_k), \quad (21b)$$

$$w_{k+1} = \arg \min_w \mathcal{L}_{\beta_1, \beta_2, k}(u_{k+1}, v_{k+1}, w, y_k, z_k), \quad (21c)$$

$$y_{k+1} = y_k + \beta_{1,k} (Au_{k+1} - v_{k+1}), \quad (21d)$$

$$z_{k+1} = z_k + \beta_{2,k} (\nabla u_{k+1} - w_{k+1}), \quad (21e)$$

$$(\beta_{1,k+1}, \beta_{2,k+1}) = \sigma(\beta_{1,k}, \beta_{2,k}), \quad (21f)$$

where $\sigma > 1$.

Remark 1. The scheme presented in (21) slightly differs from the original ADMM (Boyd et al., 2011), the latter of which has $\sigma = 1$ in (21f). Having $\sigma > 1$ increases the weights of the penalty parameters $\beta_{1,k}, \beta_{2,k}$ in each iteration k , thus accelerating the numerical convergence speed of the proposed ADMM algorithm. A similar technique has been used in Cascarano et al. (2021), Gu et al. (2017), Storath and Weinmann (2014), Storath et al. (2014), and You et al. (2019).

All the subproblems (21a)–(21c) have closed-form solutions. In particular, the first-order optimality condition for (21a) is

$$[\beta_{1,k} A^\top A - (\mu + \beta_{2,k}) \Delta] u^{k+1} = A^\top (\beta_{1,k} v_k - y_k) - \nabla^\top (z_k - \beta_{2,k} w_k), \quad (22)$$

where $\Delta = -\nabla^\top \nabla$ is the Laplacian operator. If $\ker(A) \cap \ker(\nabla) = \{0\}$, then $\beta_{1,k} A^\top A - (\mu + \beta_{2,k}) \Delta$ is positive definite and thereby invertible, which implies that (22) has a unique solution u^{k+1} . By assuming periodic boundary condition for u , the operators Δ and $A^\top A$ are block circulant (Wang et al., 2008), and hence (22) can be solved efficiently by the 2D discrete Fourier transform \mathcal{F} . Specifically, we have the formula

$$\begin{aligned} u_{k+1} &= \mathcal{F}^{-1} \left(\frac{\mathcal{F}(A)^* \circ \mathcal{F}(\beta_{1,k} v_k - y_k) - \mathcal{F}(\nabla)^* \circ \mathcal{F}(z_k - \beta_{2,k} w_k)}{\beta_{1,k} \mathcal{F}(A)^* \circ \mathcal{F}(A) - (\mu + \beta_{2,k}) \mathcal{F}(\Delta)} \right), \end{aligned} \quad (23)$$

where \mathcal{F}^{-1} is the inverse discrete Fourier transform, the superscript $*$ denotes complex conjugate, the operation \circ is componentwise multiplication, and division is componentwise. By differentiating the objective function of (21b) and setting it to zero, we can get a closed-form solution for v_{k+1} given by

$$\begin{aligned} v_{k+1} &= \frac{(\beta_{1,k} A u_{k+1} + y_k - \lambda \mathbb{1}) + \sqrt{(\beta_{1,k} A u_{k+1} + y_k - \lambda \mathbb{1})^2 + 4\lambda\beta_{1,k}}}{2\beta_{1,k}}, \end{aligned} \quad (24)$$

where the square root, squaring, and division are performed componentwise. Lastly, the w -subproblem (21c) can be decomposed componentwise as follows:

$$\begin{aligned} (w_{i,j})_{k+1} &= \arg \min_{w_{i,j}} \|w_{i,j}\|_1 - \alpha \|w_{i,j}\|_2 \\ &\quad + \frac{\beta_{2,k}}{2} \left\| w_{i,j} - \left((\nabla u_{k+1})_{i,j} + \frac{(z_k)_{i,j}}{\beta_{2,k}} \right) \right\|_2^2 \\ &= \text{prox} \left((\nabla u_{k+1})_{i,j} + \frac{(z_k)_{i,j}}{\beta_{2,k}}, \alpha, \frac{1}{\beta_{2,k}} \right), \end{aligned} \quad (25)$$

where the proximal operator for $\ell_1 - \alpha\ell_2$ on $x \in \mathbb{R}^n$ is given by

$$\text{prox}(x, \alpha, \beta) = \arg \min_y \|y\|_1 - \alpha\|y\|_2 + \frac{1}{2\beta}\|x - y\|_2^2. \quad (26)$$

The proximal operator for $\ell_1 - \alpha\ell_2$ has a closed form solution summarized by Lemma 5.

Lemma 5. (Lou and Yan, 2018) Given $x \in \mathbb{R}^n$, $\beta > 0$, and $\alpha \in [0, 1]$, the optimal solution to (26) is given by one of the following cases:

1. When $\|x\|_\infty > \beta$, we have

$$x^* = (\|\xi\|_2 + \alpha\beta) \frac{\xi}{\|\xi\|_2},$$

where $\xi = \text{sign}(x) \circ \max(|x| - \beta, 0)$.

2. When $(1 - \alpha)\beta < \|x\|_\infty \leq \beta$, then x^* is a 1-sparse vector such that one chooses $i \in \arg \max_j (|x_j|)$ and defines $x_i^* = (|x_i| + (\alpha - 1)\beta) \text{sign}(x_i)$ and the remaining elements equal to 0.
3. When $\|x\|_\infty \leq (1 - \alpha)\beta$, then $x^* = 0$.

In summary, we describe the ADMM scheme to solve (11) in Algorithm 2.

3.3. Convergence analysis

We establish the subsequential convergence of ADMM described in Algorithm 2. The global convergence of ADMM (Wang et al., 2019) is inapplicable to our model as the gradient operator ∇ is non-surjective, which will be further investigated in future work. For the sake of brevity, we set $\beta = \beta_1 = \beta_2$ and denote

$$\mathcal{L}_\beta(u, v, w, y, z) := \mathcal{L}_{\beta, \beta}(u, v, w, y, z).$$

In addition, we introduce definitions of subdifferentials (Rockafellar and Wets, 2009), which defines a stationary point of a non-smooth objective function.

Definition 6. For a proper function $h: \mathbb{R}^n \rightarrow \mathbb{R} \cup \{+\infty\}$, define $\text{dom}(h) := \{x \in \mathbb{R}^n : h(x) < +\infty\}$.

- (a) The regular subdifferential at $x \in \text{dom}(h)$ is given by

$$\hat{\partial}h(x) := \left\{ w : \liminf_{x' \rightarrow x, x' \neq x} \frac{h(x') - h(x) - \langle w, x' - x \rangle}{\|x' - x\|} \geq 0 \right\}.$$

- (b) The (limiting) subdifferential at $x \in \text{dom}(h)$ is given by

$$\partial h(x) :=$$

$$\left\{ w : \exists x_k \rightarrow x \text{ and } w_k \in \hat{\partial}h(x_k) \text{ with } w_k \rightarrow w \text{ and } h(x_k) \rightarrow h(x) \right\}.$$

An important property of the limiting subdifferential is its closedness: for any $(x_k, v_k) \rightarrow (x, v)$ with $v_k \in \partial h(x_k)$, if $h(x_k) \rightarrow h(x)$, then $v \in \partial h(x)$.

Lemma 7. Suppose that $\ker(A) \cap \ker(\nabla) = \{0\}$ and $0 \leq \alpha < 1$. Let $\{(u_k, v_k, w_k, y_k, z_k)\}_{k=1}^\infty$ be a sequence generated by Algorithm 2. Then, we have

$$\begin{aligned} & \mathcal{L}_{\beta_{k+1}}(u_{k+1}, v_{k+1}, w_{k+1}, y_{k+1}, z_{k+1}) - \mathcal{L}_{\beta_k}(u_k, v_k, w_k, y_k, z_k) \\ & \leq -\frac{\nu}{2}\|u_{k+1} - u_k\|_2^2 - \frac{\beta_0}{2}\|v_{k+1} - v_k\|_2^2 \\ & \quad + \frac{1}{\sigma^{k-1}\beta_0} \left(\|y_{k+1} - y_k\|_2^2 + \|z_{k+1} - z_k\|_2^2 \right), \end{aligned} \quad (28)$$

for some constant $\nu > 0$.

Proof. If $\ker(A) \cap \ker(\nabla) = \{0\}$, then $\beta_0 A^\top A + (\beta_0 + \mu)\nabla^\top \nabla$ is positive definite, and hence there exists $\nu > 0$ such that

$$\begin{aligned} \beta_k \|Au\|_2^2 + (\beta_k + \mu)\|\nabla u\|_2^2 & \geq \beta_0 \|Au\|_2^2 + (\beta_0 + \mu)\|\nabla u\|_2^2 \\ & \geq \nu \|u\|_2^2 \quad \forall k \in \mathbb{N}, \end{aligned}$$

which implies that $\mathcal{L}_{\beta_k}(u, v_k, w_k, y_k, z_k)$ is strongly convex with respect to u with parameter ν . Additionally, $\mathcal{L}_{\beta_k}(u_{k+1}, v, w_k, y_k, z_k)$ is strongly convex with respect to v with parameter $\beta_0 \leq \beta_k$. It follows from Beck (2017), Theorem 5.25, that we have

$$\begin{aligned} & \mathcal{L}_{\beta_k}(u_{k+1}, v_k, w_k, y_k, z_k) - \mathcal{L}_{\beta_k}(u_k, v_k, w_k, y_k, z_k) \\ & \leq -\frac{\nu}{2}\|u_{k+1} - u_k\|_2^2, \end{aligned} \quad (29)$$

$$\begin{aligned} & \mathcal{L}_{\beta_k}(u_{k+1}, v_{k+1}, w_k, y_k, z_k) - \mathcal{L}_{\beta_k}(u_{k+1}, v_k, w_k, y_k, z_k) \\ & \leq -\frac{\beta_0}{2}\|v_{k+1} - v_k\|_2^2. \end{aligned} \quad (30)$$

As w_{k+1} is the optimal solution to (21c), it is straightforward to have

$$\mathcal{L}_{\beta_k}(u_{k+1}, v_{k+1}, w_{k+1}, y_k, z_k) - \mathcal{L}_{\beta_k}(u_{k+1}, v_{k+1}, w_k, y_k, z_k) \leq 0. \quad (31)$$

Simple calculations by using (21d)–(21e) lead to

$$\begin{aligned} & \mathcal{L}_{\beta_k}(u_{k+1}, v_{k+1}, w_{k+1}, y_{k+1}, z_{k+1}) - \mathcal{L}_{\beta_k}(u_{k+1}, v_{k+1}, w_{k+1}, y_k, z_k) \\ & = (\mathcal{L}_{\beta_k}(u_{k+1}, v_{k+1}, w_{k+1}, y_{k+1}, z_{k+1}) \\ & \quad - \mathcal{L}_{\beta_k}(u_{k+1}, v_{k+1}, w_{k+1}, y_{k+1}, z_k)) \\ & \quad + (\mathcal{L}_{\beta_k}(u_{k+1}, v_{k+1}, w_{k+1}, y_{k+1}, z_k) \\ & \quad - \mathcal{L}_{\beta_k}(u_{k+1}, v_{k+1}, w_{k+1}, y_k, z_k)) \\ & = \langle z_{k+1} - z_k, \nabla u_{k+1} - w_{k+1} \rangle + \langle y_{k+1} - y_k, Au_{k+1} - v_{k+1} \rangle \\ & = \frac{1}{\beta_k} (\|y_{k+1} - y_k\|_2^2 + \|z_{k+1} - z_k\|_2^2). \end{aligned} \quad (32)$$

Lastly, we have

$$\begin{aligned} & \mathcal{L}_{\beta_{k+1}}(u_{k+1}, v_{k+1}, w_{k+1}, y_{k+1}, z_{k+1}) \\ & \quad - \mathcal{L}_{\beta_k}(u_{k+1}, v_{k+1}, w_{k+1}, y_{k+1}, z_{k+1}) \\ & = \frac{\beta_{k+1} - \beta_k}{2} (\|Au_{k+1} - v_{k+1}\|_2^2 + \|\nabla u_{k+1} - w_{k+1}\|_2^2) \\ & = \frac{\beta_{k+1} - \beta_k}{2\beta_k^2} (\|y_{k+1} - y_k\|_2^2 + \|z_{k+1} - z_k\|_2^2). \end{aligned} \quad (33)$$

```

1 Input:
  • image  $f$ 
  • blurring operator  $A$ 
  • fidelity parameter  $\lambda > 0$ 
  • smoothing parameter  $\mu \geq 0$ 
  • AITV parameter  $\alpha \in [0, 1]$ 
  • penalty parameters  $\beta_{1,0}, \beta_{2,0} > 0$ 
  • penalty multiplier  $\sigma > 1$ 
  • relative error  $\epsilon > 0$ 

2 Output:  $u_k$ 
3 Initialize  $u_0, w_0, z_0$ .
4 Set  $k = 0$ .
5 while  $\frac{\|u_k - u_{k-1}\|_2}{\|u_k\|_2} > \epsilon$  do
6

$$u_{k+1} = \mathcal{F}^{-1} \left( \frac{\mathcal{F}(A)^* \circ \mathcal{F}(\beta_{1,k} v_k - y_k) - \mathcal{F}(\nabla)^* \circ \mathcal{F}(z_k - \beta_{2,k} w_k)}{\beta_{1,k} \mathcal{F}(A)^* \circ \mathcal{F}(A) - (\mu + \beta_{2,k}) \mathcal{F}(\Delta)} \right)$$


$$v_{k+1} = \frac{(\beta_{1,k} A u_{k+1} + y_k - \lambda \mathbb{I}) + \sqrt{(\beta_{1,k} A u_{k+1} + y_k - \lambda \mathbb{I})^2 + 4\lambda\beta_{1,k}f}}{2\beta_{1,k}}$$


$$(w_{k+1})_{ij} = \text{prox} \left( (\nabla u_{k+1})_{ij} + \frac{(z_k)_{ij}}{\beta_{2,k}}, \alpha, \frac{1}{\beta_{2,k}} \right) \quad \forall (i, j) \in \Omega$$


$$y_{k+1} = y_k + \beta_{1,k} (A u_{k+1} - v_{k+1})$$


$$z_{k+1} = z_k + \beta_{2,k} (\nabla u_{k+1} - w_{k+1})$$


$$(\beta_{1,k+1}, \beta_{2,k+1}) = \sigma(\beta_{1,k}, \beta_{2,k})$$


$$k := k + 1$$


```

Algorithm 2. ADMM for the AITV-regularized smoothing model with Poisson fidelity (Equation 11).

Combining (29)–(33) together with the fact that $\beta_k = \sigma^k \beta_0$ for $\sigma > 1$, we obtain

$$\begin{aligned}
& \mathcal{L}_{\beta_{k+1}}(u_{k+1}, v_{k+1}, w_{k+1}, y_{k+1}, z_{k+1}) - \mathcal{L}_{\beta_k}(u_k, v_k, w_k, y_k, z_k) \\
& \leq -\frac{\nu}{2} \|u_{k+1} - u_k\|_2^2 - \frac{\beta_0}{2} \|v_{k+1} - v_k\|_2^2 \\
& \quad + \frac{\beta_{k+1} + \beta_k}{2\beta_k^2} \left(\|y_{k+1} - y_k\|_2^2 + \|z_{k+1} - z_k\|_2^2 \right) \\
& = -\frac{\nu}{2} \|u_{k+1} - u_k\|_2^2 - \frac{\beta_0}{2} \|v_{k+1} - v_k\|_2^2 \\
& \quad + \frac{\sigma + 1}{2\sigma^k \beta_0} \left(\|y_{k+1} - y_k\|_2^2 + \|z_{k+1} - z_k\|_2^2 \right) \\
& \leq -\frac{\nu}{2} \|u_{k+1} - u_k\|_2^2 - \frac{\beta_0}{2} \|v_{k+1} - v_k\|_2^2 \\
& \quad + \frac{1}{\sigma^{k-1} \beta_0} \left(\|y_{k+1} - y_k\|_2^2 + \|z_{k+1} - z_k\|_2^2 \right).
\end{aligned}$$

This completes the proof.

Lemma 8. Suppose that $\ker(A) \cap \ker(\nabla) = \{0\}$ and $0 \leq \alpha < 1$. Let $\{(u_k, v_k, w_k, y_k, z_k)\}_{k=1}^{\infty}$ be generated by Algorithm 2. If $\{y_k\}_{k=1}^{\infty}$ bounded, then the sequence $\{(u_k, v_k, w_k, y_k, z_k)\}_{k=1}^{\infty}$ is bounded, $u_{k+1} - u_k \rightarrow 0$, and $v_{k+1} - v_k \rightarrow 0$.

Proof. First we show that $\{z_k\}_{k=1}^{\infty}$ is bounded. Combining (21e) with the first-order optimality condition of (25), we have

$$\begin{aligned}
(z_{k+1})_{ij} &= (z_k)_{ij} + \beta_k ((\nabla u_{k+1})_{ij} - (w_{k+1})_{ij}) \\
&\in \partial (\|(w_{k+1})_{ij}\|_1 - \alpha \|(w_{k+1})_{ij}\|_2) \\
&\subseteq \partial (\|(w_{k+1})_{ij}\|_1) - \alpha \partial (\|(w_{k+1})_{ij}\|_2),
\end{aligned} \tag{34}$$

which implies that there exist $\xi_1 \in \partial \|(w_{k+1})_{ij}\|_1$ and $\xi_2 \in \partial \|(w_{k+1})_{ij}\|_2$ such that $(z_{k+1})_{ij} = \xi_1 - \alpha \xi_2$ for each $(i, j) \in \Omega$. Recall that for $x \in \mathbb{R}^2$ the subgradients of the two norms are

$$\partial \|x\|_1 = \left\{ \xi \in \mathbb{R}^2 : \xi_i = \begin{cases} \text{sign}(x_i) & \text{if } x_i \neq 0 \\ \xi_i \in [-1, 1] & \text{if } x_i = 0 \end{cases} \text{ for } i = 1, 2 \right\}, \tag{35}$$

$$\partial \|x\|_2 = \left\{ \xi \in \mathbb{R}^2 : \xi = \begin{cases} \frac{x}{\|x\|_2} & \text{if } x \neq 0 \\ \in \{\xi \in \mathbb{R}^2 : \|\xi\|_2 \leq 1\} & \text{if } x = 0 \end{cases} \right\}. \tag{36}$$

Therefore, we have $\|\xi_1\|_{\infty} \leq 1$, $\|\xi_2\|_{\infty} \leq 1$, and hence $\|(z_{k+1})_{ij}\|_{\infty} \leq 1 + \alpha$ (by the triangle inequality), i.e., $\{z_k\}_{k=1}^{\infty}$ is bounded.

By the assumption $\{y_k\}_{k=1}^{\infty}$ is bounded. There exist two constants $C_1, C_2 > 0$ such that $\|y_{k+1} - y_k\|_2^2 \leq C_1$, $\|z_{k+1} - z_k\|_2^2 \leq$

C_1 , $\|y_k\|_2^2 \leq C_2$, and $\|z_k\|_2^2 \leq C_2$ for all $k \in \mathbb{N}$. Hence, we have from (28) that

$$\begin{aligned} \mathcal{L}_{\beta_{k+1}}(u_{k+1}, v_{k+1}, w_{k+1}, y_{k+1}, z_{k+1}) &\leq \\ \mathcal{L}_{\beta_k}(u_k, v_k, w_k, y_k, z_k) - \frac{\nu}{2} \|u_{k+1} - u_k\|_2^2 \\ - \frac{\beta_0}{2} \|v_{k+1} - v_k\|_2^2 + \frac{2C_1}{\sigma^{k-1} \beta_0}. \end{aligned} \quad (37)$$

A telescoping summation of (37) leads to

$$\begin{aligned} \mathcal{L}_{\beta_{k+1}}(u_{k+1}, v_{k+1}, w_{k+1}, y_{k+1}, z_{k+1}) &\leq \\ \mathcal{L}_{\beta_0}(u_0, v_0, w_0, y_0, z_0) + \frac{2C_1}{\beta_0} \sum_{i=0}^k \frac{1}{\sigma^{i-1}} \\ - \frac{\nu}{2} \sum_{i=0}^k \|u_{i+1} - u_i\|_2^2 - \frac{\beta_0}{2} \sum_{i=0}^k \|v_{i+1} - v_i\|_2^2. \end{aligned} \quad (38)$$

By completing two least-squares terms, we can rewrite $\mathcal{L}_{\beta_{k+1}}$ as

$$\begin{aligned} \mathcal{L}_{\beta_{k+1}}(u_{k+1}, v_{k+1}, w_{k+1}, y_{k+1}, z_{k+1}) &= \lambda \langle v_{k+1} - f \log v_{k+1}, \mathbb{1} \rangle + \frac{\mu}{2} \|\nabla u_{k+1}\|_2^2 \\ &\quad + \|w_{k+1}\|_1 - \alpha \|w_{k+1}\|_{2,1} \\ &\quad + \frac{\beta_{k+1}}{2} \left\| Au_{k+1} - v_{k+1} + \frac{y_{k+1}}{\beta_{k+1}} \right\|_2^2 - \frac{\|y_{k+1}\|_2^2}{2\beta_{k+1}} \\ &\quad + \frac{\beta_{k+1}}{2} \left\| \nabla u_{k+1} - w_{k+1} + \frac{z_{k+1}}{\beta_{k+1}} \right\|_2^2 - \frac{\|z_{k+1}\|_2^2}{2\beta_{k+1}}. \end{aligned} \quad (39)$$

Combining (38) and (39), we have

$$\begin{aligned} \lambda \langle f - f \log f, \mathbb{1} \rangle + (1 - \alpha) \|w_{k+1}\|_1 - \frac{C_2}{\beta_0} \\ \leq \mathcal{L}_{\beta_{k+1}}(u_{k+1}, v_{k+1}, w_{k+1}, y_{k+1}, z_{k+1}) \\ \leq \mathcal{L}_{\beta_0}(u_0, v_0, w_0, y_0, z_0) + \frac{2C_1}{\beta_0} \sum_{i=0}^k \frac{1}{\sigma^{i-1}} \\ - \frac{\nu}{2} \sum_{i=0}^k \|u_{i+1} - u_i\|_2^2 - \frac{\beta_0}{2} \sum_{i=0}^k \|v_{i+1} - v_i\|_2^2 \\ \leq \mathcal{L}_{\beta_0}(u_0, v_0, w_0, y_0, z_0) + \frac{2C_1}{\beta_0} \sum_{i=0}^{\infty} \frac{1}{\sigma^{i-1}}. \end{aligned} \quad (40)$$

Since $\sigma > 1$, the infinite sum is finite, and hence we have $\forall k \in \mathbb{N}$,

$$\begin{aligned} \|w_{k+1}\|_1 &\leq \frac{1}{1 - \alpha} \left(\mathcal{L}_{\beta_0}(u_0, v_0, w_0, y_0, z_0) \right. \\ &\quad \left. - \lambda \langle f - f \log f, \mathbb{1} \rangle + \frac{2C_1}{\beta_0} \sum_{i=0}^{\infty} \frac{1}{\sigma^{i-1}} + \frac{C_2}{\beta_0} \right) < \infty, \end{aligned}$$

which implies that $\{w_k\}_{k=1}^{\infty}$ is bounded. Also from (38) and (39), we have

$$\begin{aligned} \lambda \langle f - f \log f, \mathbb{1} \rangle - \frac{C_2}{\beta_0} &\leq \lambda \langle v_{k+1} - f \log v_{k+1}, \mathbb{1} \rangle - \frac{C_2}{\beta_0} \\ &\leq \lambda \langle v_{k+1} - f \log v_{k+1}, \mathbb{1} \rangle - \frac{\|y_{k+1}\|_2^2}{2\beta_{k+1}} - \frac{\|z_{k+1}\|_2^2}{2\beta_{k+1}} \\ &\leq \mathcal{L}_{\beta_{k+1}}(u_{k+1}, v_{k+1}, w_{k+1}, y_{k+1}, z_{k+1}) \end{aligned}$$

$$\leq \mathcal{L}_{\beta_0}(u_0, v_0, w_0, y_0, z_0) + \frac{2C_1}{\beta_0} \sum_{i=0}^{\infty} \frac{1}{\sigma^{i-1}} < \infty.$$

This shows that $\{\langle v_k - f \log v_k, \mathbb{1} \rangle\}_{k=1}^{\infty}$ is bounded. By emulating the computation in (18), it can be shown that $\{v_k\}_{k=1}^{\infty}$ is bounded.

It suffices to prove that $\{(Au_k, \nabla u_k)\}_{k=1}^{\infty}$ is bounded in order to prove the boundedness of $\{u_k\}_{k=1}^{\infty}$ by Proposition 3. Using (21d), we have

$$\|Au_{k+1}\|_2 \leq \frac{\|y_{k+1} - y_k\|_2}{\beta_k} + \|v_{k+1}\|_2 \leq \frac{\sqrt{C_1}}{\beta_0} + \|v_{k+1}\|_2.$$

As $\{v_k\}_{k=1}^{\infty}$ is proven to be bounded, then $\{Au_k\}_{k=1}^{\infty}$ is also bounded. We can prove $\{\nabla u_k\}_{k=1}^{\infty}$ is bounded similarly using (21e). Altogether, $\{(u_k, v_k, w_k, y_k, z_k)\}_{k=1}^{\infty}$ is bounded.

It follows from (40) that

$$\begin{aligned} \frac{\nu}{2} \sum_{i=0}^k \|u_{i+1} - u_i\|_2^2 + \frac{\beta_0}{2} \sum_{i=0}^k \|v_{i+1} - v_i\|_2^2 &\leq \mathcal{L}_{\beta_0}(u_0, v_0, w_0, y_0, z_0) \\ + \frac{2C_1}{\beta_0} \sum_{i=0}^k \frac{1}{\sigma^{i-1}} - \lambda \langle f - f \log f, \mathbb{1} \rangle + \frac{C_2}{\beta_0}. \end{aligned}$$

As $k \rightarrow \infty$, we see the right-hand side is finite, which forces the infinite summations on the left-hand side to converge, and hence we have $u_{k+1} - u_k \rightarrow 0$ and $v_{k+1} - v_k \rightarrow 0$.

Theorem 9. Suppose that $\ker(A) \cap \ker(\nabla) = \{0\}$ and $0 \leq \alpha < 1$. Let $\{(u_k, v_k, w_k, y_k, z_k)\}_{k=1}^{\infty}$ be generated by Algorithm 2. If $\{y_k\}_{k=1}^{\infty}$ bounded, $\beta_k(v_{k+1} - v_k) \rightarrow 0$, $\beta_k(w_{k+1} - w_k) \rightarrow 0$, $y_{k+1} - y_k \rightarrow 0$, and $z_{k+1} - z_k \rightarrow 0$, then there exists a subsequence whose limit point $(u^*, v^*, w^*, y^*, z^*)$ is a stationary point of (19) that satisfies the following:

$$0 = -\mu \Delta u^* + A^T y^* + \nabla^T z^*, \quad (41a)$$

$$0 = \lambda \left(\mathbb{1} - \frac{f}{v^*} \right) - y^*, \quad (41b)$$

$$z^* \in \partial (\|w^*\|_1 - \alpha \|w^*\|_{2,1}), \quad (41c)$$

$$Au^* = v^*, \quad (41d)$$

$$\nabla u^* = w^*. \quad (41e)$$

Proof. By Lemma 8, the sequence $\{(u_k, v_k, w_k, y_k, z_k)\}_{k=1}^{\infty}$ is bounded, so there exists a subsequence $\{(u_{k_n}, v_{k_n}, w_{k_n}, y_{k_n}, z_{k_n})\}_{n=1}^{\infty}$ that converges to a point $(u^*, v^*, w^*, y^*, z^*)$. Additionally, we have $u_{k+1} - u_k \rightarrow 0$ and $v_{k+1} - v_k \rightarrow 0$. Since $\{y_k, z_k\}_{k=1}^{\infty}$ is bounded, there exists a constant $C > 0$ such that $\|y_{k+1} - y_k\|_2 < C$ and $\|z_{k+1} - z_k\|_2 < C$ for each $k \in \mathbb{N}$. By (21e), we have

$$\begin{aligned} \|w_{k+1} - w_k\|_2 &\leq \|w_{k+1} - \nabla u_{k+1}\|_2 + \|\nabla u_{k+1} - \nabla u_k\|_2 \\ &\quad + \|\nabla u_k - w_k\|_2 \\ &= \frac{\|z_{k+1} - z_k\|_2}{\beta_k} + \|\nabla u_{k+1} - \nabla u_k\|_2 \\ &\quad + \frac{\|z_k - z_{k-1}\|_2}{\beta_{k-1}} \end{aligned}$$

$$\leq \frac{2C}{\beta_{k-1}} + \|\nabla u_{k+1} - \nabla u_k\|_2.$$

As $k \rightarrow \infty$, we have $w_{k+1} - w_k \rightarrow 0$. Altogether, we can derive the following results:

$$\lim_{n \rightarrow \infty} (u_{k_n+1}, v_{k_n+1}, w_{k_n+1}) = \lim_{n \rightarrow \infty} (u_{k_n}, v_{k_n}, w_{k_n}) = (u^*, v^*, w^*). \quad (42)$$

Furthermore, the assumptions give us

$$\begin{aligned} \lim_{n \rightarrow \infty} \beta_{k_n} (v_{k_n+1} - v_{k_n}) &= 0, \\ \lim_{n \rightarrow \infty} \beta_{k_n} (w_{k_n+1} - w_{k_n}) &= 0, \\ \lim_{n \rightarrow \infty} y_{k_n+1} - y_{k_n} &= 0, \\ \lim_{n \rightarrow \infty} z_{k_n+1} - z_{k_n} &= 0. \end{aligned}$$

By (21d)–(21e), we have

$$\begin{aligned} \|Au^* - v^*\|_2 &= \lim_{n \rightarrow \infty} \|Au_{k_n+1} - v_{k_n+1}\|_2 \\ &= \lim_{n \rightarrow \infty} \frac{\|y_{k_n+1} - y_{k_n}\|_2}{\beta_{k_n}} \leq \lim_{n \rightarrow \infty} \frac{C}{\beta_{k_n}} = 0, \\ \|\nabla u^* - w^*\|_2 &= \lim_{n \rightarrow \infty} \|\nabla u_{k_n+1} - w_{k_n+1}\|_2 \\ &= \lim_{n \rightarrow \infty} \frac{\|z_{k_n+1} - z_{k_n}\|_2}{\beta_{k_n}} \leq \lim_{n \rightarrow \infty} \frac{C}{\beta_{k_n}} = 0. \end{aligned}$$

Hence, we have $Au^* = v^*$ and $\nabla u^* = w^*$.

The optimality conditions at iteration k_n are the following:

$$\begin{aligned} -\mu \Delta u_{k_n+1} + A^\top y_{k_n} + \beta_{k_n} A^\top (Au_{k_n+1} - v_{k_n}) \\ + \nabla^\top z_{k_n} + \beta_{k_n} \nabla^\top (\nabla u_{k_n+1} - w_{k_n}) = 0, \end{aligned} \quad (43a)$$

$$\lambda \left(\mathbb{I} - \frac{f}{v_{k_n+1}} \right) - y_{k_n} - \beta_{k_n} (Au_{k_n+1} - v_{k_n+1}) = 0, \quad (43b)$$

$$z_{k_n} + \beta_{k_n} (\nabla u_{k_n+1} - w_{k_n+1}) \in \partial (\|w_{k_n+1}\|_1 - \alpha \|w_{k_n+1}\|_{2,1}). \quad (43c)$$

Expanding (43a) by substituting in (21d)–(21e) and taking the limit, we have

$$\begin{aligned} 0 &= \lim_{n \rightarrow \infty} -\mu \Delta u_{k_n+1} + A^\top y_{k_n} + \beta_{k_n} A^\top (Au_{k_n+1} - v_{k_n}) \\ &\quad + \nabla^\top z_{k_n} + \beta_{k_n} \nabla^\top (\nabla u_{k_n+1} - w_{k_n}) \\ &= \lim_{n \rightarrow \infty} -\mu \Delta u_{k_n+1} + A^\top y_{k_n} + \beta_{k_n} A^\top (Au_{k_n+1} - v_{k_n+1}) \\ &\quad + \beta_{k_n} A^\top (v_{k_n+1} - v_{k_n}) + \nabla^\top z_{k_n} \\ &\quad + \beta_{k_n} \nabla^\top (\nabla u_{k_n+1} - w_{k_n+1}) \\ &\quad + \beta_{k_n} \nabla^\top (w_{k_n+1} - w_{k_n}) \\ &= \lim_{n \rightarrow \infty} -\mu \Delta u_{k_n+1} + A^\top y_{k_n} + A^\top (y_{k_n+1} - y_{k_n}) \\ &\quad + \beta_{k_n} A^\top (v_{k_n+1} - v_{k_n}) + \nabla^\top z_{k_n} \\ &\quad + \nabla^\top (z_{k_n+1} - z_{k_n}) + \beta_{k_n} \nabla^\top (w_{k_n+1} - w_{k_n}) \\ &= -\mu \Delta u^* + A^\top y^* + \nabla^\top z^*. \end{aligned}$$

Substituting in (21d) into (43b) and taking the limit give us

$$0 = \lim_{n \rightarrow \infty} \lambda \left(\mathbb{I} - \frac{f}{v_{k_n+1}} \right) - y_{k_n} - \beta_{k_n} (Au_{k_n+1} - v_{k_n+1})$$

$$\begin{aligned} &= \lim_{n \rightarrow \infty} \lambda \left(\mathbb{I} - \frac{f}{v_{k_n+1}} \right) - y_{k_n} - (y_{k_n+1} - y_{k_n}) \\ &= \lambda \left(\mathbb{I} - \frac{f}{v^*} \right) - y^*. \end{aligned}$$

Lastly, by substituting (21e) into (43c), we have

$$z_{k_n+1} \in \partial (\|w_{k_n+1}\|_1 - \alpha \|w_{k_n+1}\|_{2,1}).$$

By continuity, we have $\|w_{k_n+1}\|_1 - \alpha \|w_{k_n+1}\|_{2,1} \rightarrow \|w^*\|_1 - \alpha \|w^*\|_{2,1}$. Together with the fact that $(w_{k_n+1}, z_{k_n+1}) \rightarrow (w^*, z^*)$, we have $z^* \in \partial (\|w^*\|_1 - \alpha \|w^*\|_{2,1})$ by closedness of the subdifferential.

Therefore, $(u^*, v^*, w^*, y^*, z^*)$ is a stationary point.

Remark 2. It is true that the assumptions in Theorem 9 are rather strong, but they are standard in the convergence analyses of other ADMM algorithms for nonconvex problems that fail to satisfy the conditions for global convergence in Wang et al. (2019). For example, Jung (2017), Jung et al. (2014), Li et al. (2016) and Li Y. et al. (2020) assumed convergence of the successive differences of the primal variables and Lagrange multipliers. Instead, we modify the convergence of the successive difference of the primal variables, i.e., $\beta_k (v_{k+1} - v_k) \rightarrow 0$, $\beta_k (w_{k+1} - w_k) \rightarrow 0$. Boundedness of the Lagrange multiplier (i.e., $\{y_k\}_{k=1}^\infty$) was also assumed in Liu et al. (2022) and Xu Y. et al. (2012), which required a stronger assumption than ours regarding the successive difference of the Lagrange multipliers.

4. Numerical experiments

In this section, we apply the proposed method of AITV Poisson SaT/SLaT on various grayscale and color images for image segmentation. For grayscale images, we compare our method with the original TV SaT (Chan et al., 2014), thresholded-Rudin-Osher-Fatemi (T-ROF) (Cai et al., 2019), and the Potts model (Potts, 1952) solved by either Pock's algorithm (Pock) (Pock et al., 2009) or Storath and Weinmann's algorithm (Storath) (Storath and Weinmann, 2014). For color images, we compare with TV SLAT (Cai et al., 2017), Pock's method (Pock et al., 2009), and Storath's method (Storath and Weinmann, 2014). We can solve (9) for TV SaT/SLaT via Algorithm 2 that utilizes the proximal operator corresponding to the $\|\cdot\|_{2,1}$ norm. The code for T-ROF is provided by the respective author¹ and we can adapt it to handle blur by using a more general data fidelity term. Pock's method is implemented by the lab group². Storath's method is provided by the original author³. Note that T-ROF, Pock's method, and Storath's method are designed for images corrupted with Gaussian noise. We apply the Anscombe transform (Anscombe, 1948) to the test images, after which the Poisson noise becomes approximately Gaussian noise. Since Storath's method is not for segmentation, we perform a

¹ <https://xiaoahaochai.netlify.app/download/>

² Python code is available at <https://github.com/VLOGroup/pgmo-lecture/blob/master/notebooks/tv-potts.ipynb> and a translated MATLAB code is available at https://github.com/kbui1993/MATLAB_Potts.

³ <https://github.com/mstorath/Pottslab>

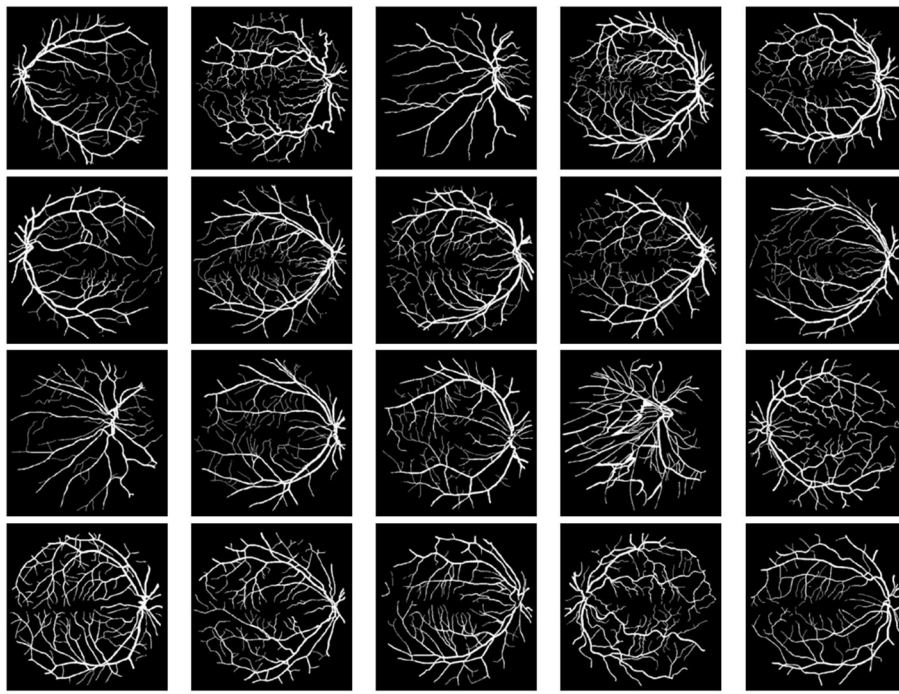


FIGURE 1

The entire DRIVE dataset (Staal et al., 2004) for binary segmentation. The image size is 584×565 with background value of 200 and the pixel value for vessels to be 255.

post-processing step of k -means clustering to its piecewise-constant output. For the SLaT methods, we parallelize the smoothing step separately for each channel.

To quantitatively measure the segmentation performance, we use the DICE index (Dice, 1945) and peak signal-to-noise ratio (PSNR). Let $S \subset \Omega$ be the ground-truth region and $S' \subset \Omega$ be a region obtained from the segmentation algorithm corresponding to the ground-truth region S . The DICE index is formulated by

$$\text{DICE} = \frac{2|S \cap S'|}{|S| + |S'|}.$$

To compare the piecewise-constant reconstruction \tilde{f} according to (10) with the original test image f , we compute PSNR by

$$\text{PSNR} = 20 \log_{10} \frac{(M \times N) \times P}{\sum_{i,j} (f_{i,j} - \tilde{f}_{i,j})^2},$$

where $M \times N$ is the image size and $P = \max_{i,j} f_{i,j}$.

Poisson noise is added to the test images by the MATLAB command `poissrnd`. To ease parameter tuning, we scale each test image to $[0, 1]$ after its degradation with Poisson noise and/or blur. We set $\sigma = 1.25$ and $\beta_{1,0} = \beta_{2,0} = 1.0, 2.0$ in [Algorithm 2](#) for grayscale and color images, respectively. The stopping criterion is either 300 iterations or when the relative error of u_k is below $\epsilon = 10^{-4}$. We tune the fidelity parameter λ and the smoothing parameter μ for each image, which will be specified later. For T-ROF, Pock's method, and Storath's method, their parameters are manually tuned to give the best DICE indices for binary segmentation (Section 4.1) and the PSNR values for multiphase

segmentation (Sections 4.2-4.3). All experiments are performed in MATLAB R2022b on a Dell laptop with a 1.80 GHz Intel Core i7-8565U processor and 16.0 GB RAM.

4.1. Grayscale, binary segmentation

We start with performing binary segmentation on the entire DRIVE dataset (Staal et al., 2004) that consists of 20 images shown in [Figure 1](#). Each image has size 584×565 with modified pixel values of either 200 for the background or 255 for the vessels. Before adding Poisson noise, we set the peak value of the image to be $P/2$ or $P/5$, where $P = 255$. Note that a lower peak value indicates stronger noise in the image, thus more challenging for denoising. We examine three cases: (1) $P/2$ no blur, (2) $P/5$ no blur, and (3) $P/2$ with Gaussian blur specified by MATLAB command `fspecial("gaussian," [10 10], 2)`. For the TV SaT method, we set $\lambda = 14.5$, $\mu = 0.5$ for case (1), $\lambda = 8.0$, $\mu = 0.5$ for case (2), and $\lambda = 22.5$, $\mu = 0.25$ for case (3). For the AITV SaT method, the parameters λ and μ are set the same as TV SaT, and we have $\alpha = 0.3$ for cases (1)–(2) and $\alpha = 0.8$ for case (3).

[Table 1](#) records the DICE indices and the computational time in seconds for the competing methods, averaged over 20 images. We observe that AITV SaT attains the best DICE indices for all three cases with comparable computational time to TV SaT and T-ROF, all of which are much faster than Pock and Storath. As visually illustrated in [Figure 2](#), AITV SaT segments more of the thinner vessels compared to TV SaT and T-ROF in five images, thereby having the higher average DICE indices.

TABLE 1 DICE and computational time in seconds of the binary segmentation methods averaged over 20 images in Figure 1 with standard deviations in parentheses.

		TV SaT	AITV SaT	T-ROF	Pock	Storath
P/2 no blur	DICE	0.9464 (0.0091)	0.9501 (0.0076)	0.9463 (0.0073)	0.8466 (0.0301)	0.8855 (0.0181)
	Time (sec.)	4.2401 (0.3618)	5.7342 (0.5251)	4.9206 (1.4281)	24.7376 (3.2454)	19.9456 (1.8875)
P/5 no blur	DICE	0.8714 (0.0134)	0.8735 (0.0125)	0.8570 (0.0170)	0.6504 (0.0910)	0.8277 (0.0191)
	Time (sec.)	4.7076 (0.6937)	6.4027 (0.8441)	5.4943 (0.7935)	46.9346 (9.4969)	21.8734 (2.7660)
P/2 with Gaussian Blur	DICE	0.7244 (0.0254)	0.7411 (0.0220)	0.7322 (0.0251)	0.5473 (0.0398)	0.6944 (0.0217)
	Time (sec.)	7.4495 (1.0983)	9.2523 (1.5959)	11.7337 (2.1252)	47.3911 (10.9191)	19.9444 (2.4142)

Bold indicates best result.

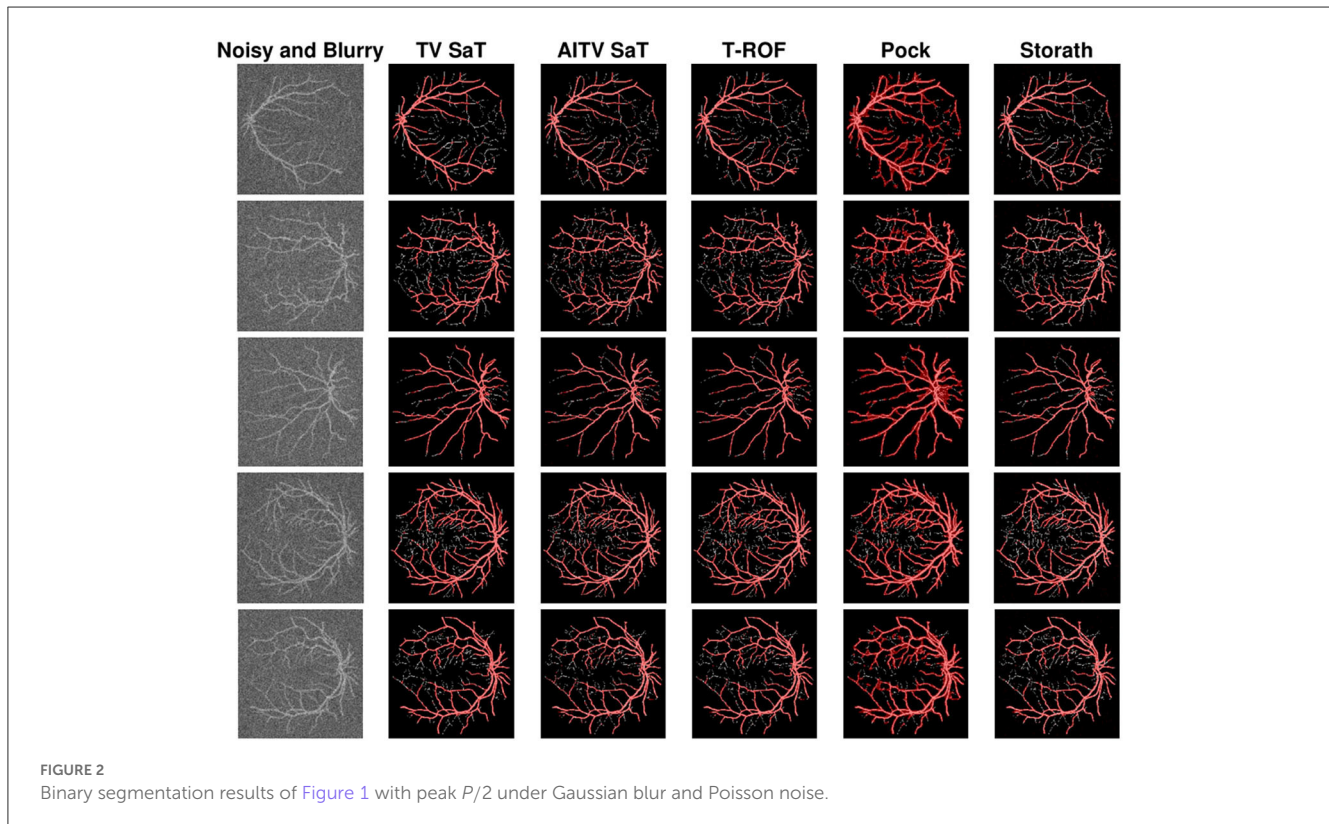


FIGURE 2
Binary segmentation results of Figure 1 with peak P/2 under Gaussian blur and Poisson noise.

4.2. Grayscale, multiphase segmentation

We examine the multiphase segmentation on the entire BrainWeb dataset (Aubert-Broche et al., 2006) that consists of 20 grayscale images as shown in Figure 3. Each image is of size 104 × 87 and has four regions to segment: background, cerebrospinal fluid (CSF), gray matter (GM), and white matter (WM). The pixel values are 10 (background), 48 (CSF), 106 (GM), and 154 (WM). The maximum intensity $P = 154$. We consider two cases: (1) $P/2$ no blur and (2) $P/2$ with motion blur specified by `fspecial("motion," 5, 225)`. For the SaT methods, we have $\mu = 1.0$, $\alpha = 0.6, 0.7$, and $\lambda = 4.0, 5.0$ for case (1) and case (2), respectively.

Across all 20 images of the BrainWeb dataset, Table 2 reports the average DICE indices for CSF, GM, and WM and average

computational times in seconds of the segmentation methods. For both cases (1) and (2), AITV SaT attains the highest average DICE indices for segmenting CSF, GM, and WM. AITV SaT is comparable to TV SaT and T-ROF in terms of computational time.

Figure 4 shows the segmentation results of the first image in Figure 3 for case (1). When segmenting CSF, the methods (TV SaT, AITV SaT, and Storath) yield similar visual results, while Pock fails to segment roughly half of the region. In addition, AITV SaT segments the most GM region with the least amount of noise artifacts than the other methods. Lastly, for WM segmentation, AITV SaT avoids the “holes” or “gaps” and segments fewer regions outside of the ground truth, thus outperforming TV SaT and Storath. For the three regions, T-ROF has the most noise artifacts in its segmentation results.

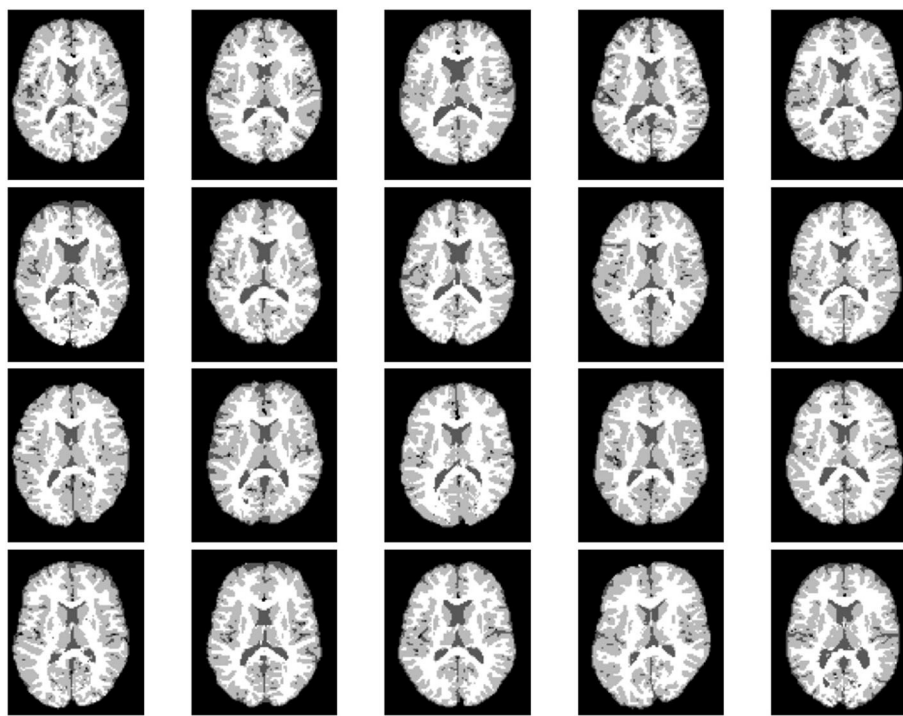


FIGURE 3

The entire BrainWeb dataset (Aubert-Broche et al., 2006) for grayscale, multiphase segmentation. Each image is of size 104×87 . The pixel values are 10 (background), 48 (cerebrospinal fluid), 106 (gray matter), and 154 (white matter).

TABLE 2 DICE and computational time in seconds of the multiphase segmentation methods averaged over 20 images in Figure 3 with standard deviations in parentheses.

		TV SaT	AITV SaT	T-ROF	Pock	Storath
P/8 no blur	CSF DICE	0.8208 (0.0270)	0.8396 (0.0262)	0.7398 (0.1316)	0.4572 (0.1474)	0.8041 (0.0244)
	GM DICE	0.8097 (0.0258)	0.8477 (0.0157)	0.7904 (0.0422)	0.7507 (0.0719)	0.7900 (0.0344)
	WM DICE	0.8449 (0.0125)	0.8694 (0.0101)	0.8221 (0.0132)	0.8459 (0.0283)	0.8138 (0.0196)
	Time (sec.)	0.2607 (0.0625)	0.2863 (0.0470)	0.2202 (0.0324)	2.6139 (0.6690)	0.3383 (0.0948)
P/8 with Motion Blur	CSF DICE	0.6196 (0.0385)	0.6260 (0.0483)	0.6174 (0.0460)	0.3772 (0.0561)	0.4964 (0.0468)
	GM DICE	0.6809 (0.0304)	0.7138 (0.0262)	0.6528 (0.0358)	0.6345 (0.0590)	0.6544 (0.0399)
	WM DICE	0.7757 (0.0127)	0.7935 (0.0110)	0.7686 (0.0164)	0.7529 (0.0185)	0.7382 (0.0140)
	Time (sec.)	0.2494 (0.0443)	0.2854 (0.0279)	0.3647 (0.0693)	2.5782 (0.4683)	0.3052 (0.1399)

Bold indicates best result.

4.3. Color segmentation

We perform color image segmentation on 10 images shown in Figure 5, which are selected from the PASCAL VOC 2010 dataset (Everingham et al., 2009). Each image has six different color regions. Figure 5A is of size 307×461 ; Figure 5B is of 500×367 ; Figures 5C, H, I are of 500×375 ; and Figures 5D–G, J are of 375×500 . Before adding Poisson noise to each channel of each image, we set the peak value $P = 10$. We choose the parameters of the SLAT methods to be $\lambda = 1.5$, $\mu = 0.05$, and $\alpha = 0.6$.

Figures 6, 7 present the piecewise-constant approximations via (10), showing similar segmentation results obtained by

TV SLAT, AITV SLAT, and Storath. Quantitatively in Table 3, AITV SLAT has better PSNRs than TV SLAT and Pock for all the images and outperforms Storath for seven. Overall, the proposed AITV SLAT has the highest PSNR on average over 10 images with the lowest standard deviation and comparable speed as Storath.

4.4. Parameter analysis

The proposed smoothing model (11) involves the following parameters:

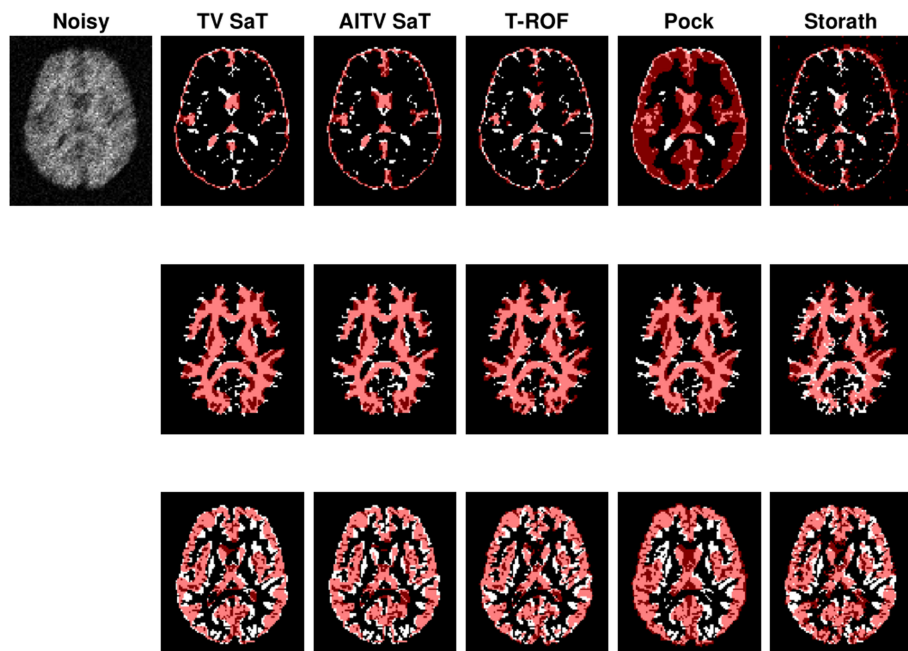


FIGURE 4

Segmentation result of the first image of [Figure 3](#) with peak $P/8$ under Poisson noise with no blur. From top to bottom are segmentation results for CSF, GM, and WM.

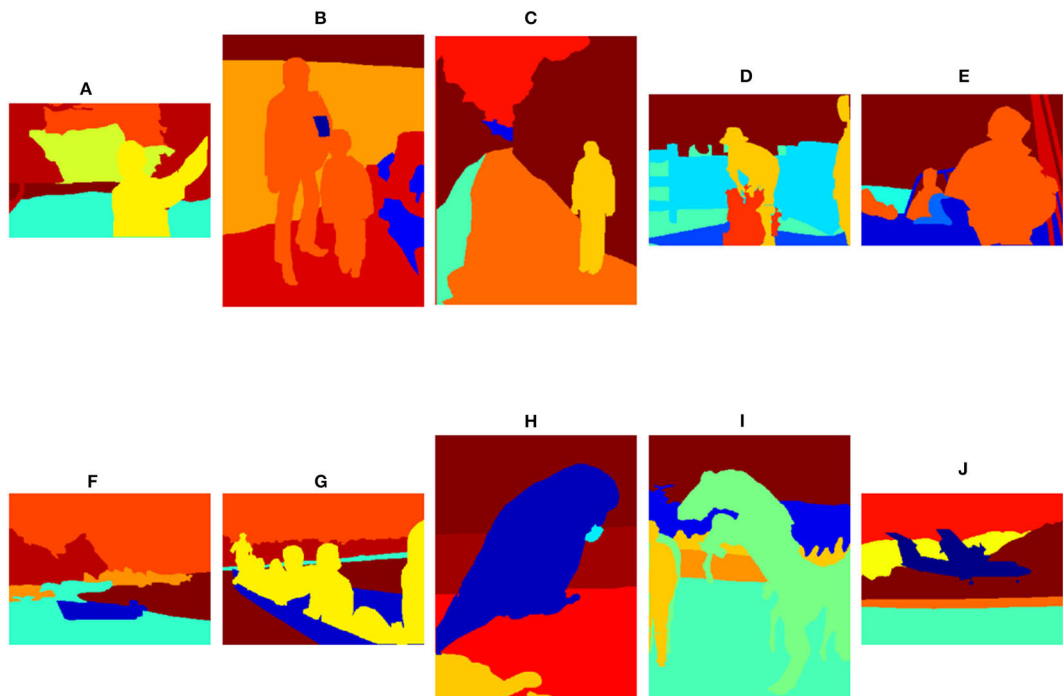


FIGURE 5

Test images from the PASCAL VOC 2010 dataset ([Everingham et al., 2009](#)) for color, multiphase segmentation. Each image has six regions. The image sizes are (A) 307×461 , (B) 500×367 , (C) 500×375 , (D–G) 375×500 , (H, I) 500×375 , and (J) 375×500 .

- The fidelity parameter λ weighs how close the approximation Au^* is to the original image f . For a larger amount of noise, the value of λ should be chosen smaller.
- The smoothing parameter μ determines how smooth the solution u^* should be. A larger value of μ may improve denoising, but at a cost of smearing out the edges between

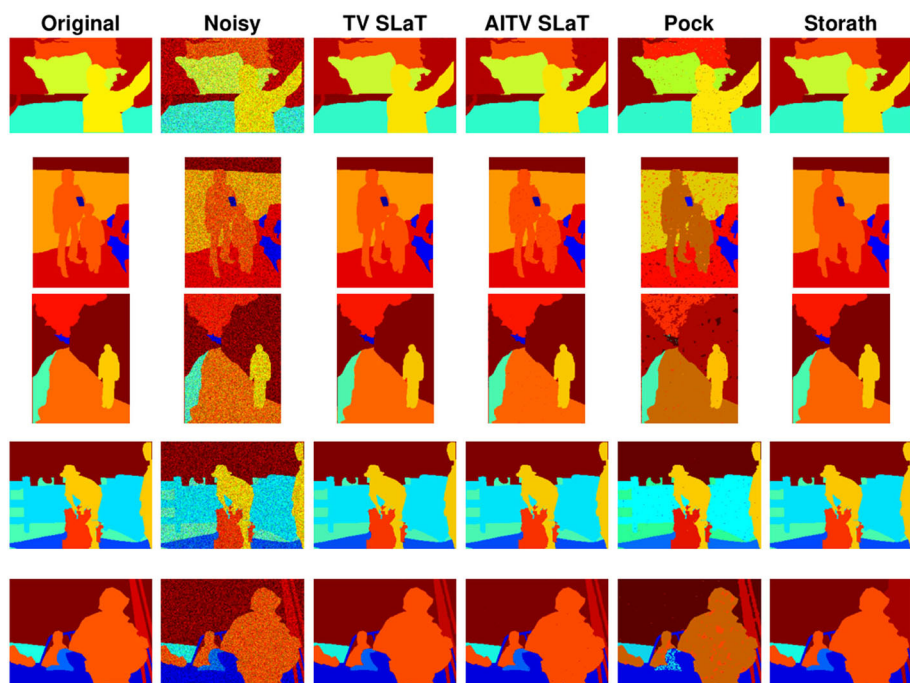


FIGURE 6
Color image segmentation results of Figures 5A–E.

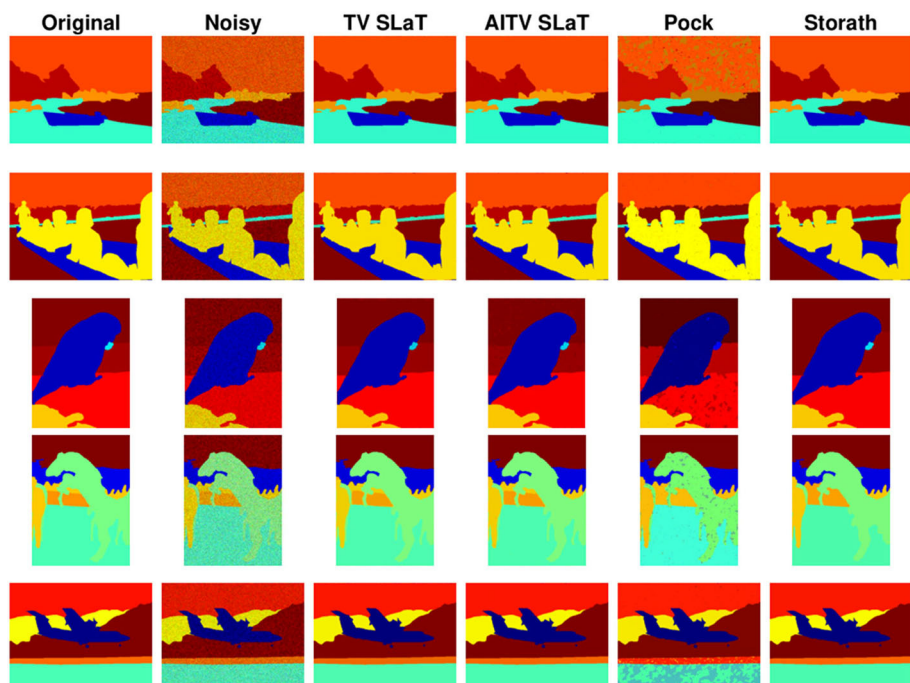


FIGURE 7
Color image segmentation results of Figures 5F–J.

adjacent regions, which may be segmented together if they have similar colors.

- The sparsity parameter $\alpha \in [0, 1]$ determines how sparse the gradient vector at each pixel should be. More specifically,

the closer the value α is to 1, the more $\|\nabla u\|_1 - \alpha \|\nabla u\|_2$ resembles $\|\nabla u\|_0$.

We perform sensitivity analysis on these parameters to understand how they affect the segmentation quality of AITV SaT/SLaT. We consider two types of tests in the case of $P/8$ with motion blur in Figure 3. In the first case (Figure 8), we fix $\mu = 1.0$ and vary α, λ . In the second case (Figure 9), we fix $\lambda = 5.0$ and vary α, μ . Figure 8 reveals a concave relationship of the DICE index of each region with respect to the parameter λ , which implies there exists the optimal choice of λ . Additionally, when λ is small, a large value for α can improve the DICE indices. According to Figure 9, the DICE indices of the GM and WM regions decrease with respect to μ , while the DICE index of the CSF region is approximately constant. For $\alpha = 0.8$, the DICE indices of the GM and WM regions are the largest when $\mu \geq 1$, but the large α is not optimal for CSF. Hence, an intermediate value of α , such as 0.6, is preferable to attain satisfactory segmentation quality for all three regions.

Lastly, in Figure 10, we conduct sensitive analysis for the case of $P = 10$ of Figure 5. We fix $\mu = 0.05$, while varying λ, α in Figure 10A, which indicates that the optimal value for α is in the range of $0.5 \leq \alpha \leq 0.7$. Then we fix $\lambda = 1.5$ to examine μ and α in Figure 10B. For $0.2 \leq \alpha \leq 0.7$, PSNR decreases as μ increases. Again, $\alpha = 0.6$ generally yields the best PSNR.

5. Conclusion and future work

In this paper, we developed the AITV Poisson SaT/SLaT framework for image segmentation. In particular, we proposed a simplified Mumford-Shah model with the AITV regularization and Poisson fidelity for the smoothing step. The model was proven to have a global minimizer. Our numerical algorithm incorporated a specific splitting scheme for ADMM and the $\ell_1 - \alpha \ell_2$ proximal operator for solving a subproblem. Convergence analysis established that the sequence generated by ADMM has a convergent subsequence to a stationary point of the nonconvex model. In our numerical experiments, the AITV Poisson SaT/SLaT yielded high-quality segmentation results within seconds for various grayscale and color images corrupted with Poisson noise and/or blur. For future directions, we are interested in other

nonconvex regularization, such as ℓ_1/ℓ_2 on the gradient (Wang et al., 2021, 2022; Wu et al., 2022a), $\ell_p, 0 < p < 1$, on the gradient (Hintermüller and Wu, 2013; Li Y. et al., 2020; Wu et al., 2021b), and transformed total variation (Huo et al., 2022), as alternatives to AITV. On the other hand, we can develop AITV variants of weighted TV (Li and Li, 2022) or adaptive TV (Wu et al., 2021a;

TABLE 3 PSNR and computation time in seconds for color image segmentation of the images in Figure 5.

		TV SLaT	AITV SLaT	Pock	Storath
PSNR	Figure 5A	29.0337	30.4619	19.2306	28.7141
	Figure 5B	31.8673	31.7055	17.3512	30.9703
	Figure 5C	30.9605	33.4217	18.0389	32.2217
	Figure 5D	29.5265	32.5505	21.4873	34.7881
	Figure 5E	29.8903	31.0656	19.7646	28.3456
	Figure 5F	33.2308	34.7619	17.9788	34.4106
	Figure 5G	28.1136	30.6237	22.5048	31.2439
	Figure 5H	33.2682	33.4250	18.9390	31.9377
	Figure 5I	30.0659	31.7937	20.0856	29.3905
	Figure 5J	31.4164	34.0610	20.3185	34.3599
Avg. (Std.)	30.7373 (1.7266)	32.3870 (1.4905)	19.5700 (1.6147)	31.6383 (2.3686)	
Time (sec.)	Figure 5A	7.1992	8.2455	148.9232	4.9410
	Figure 5B	12.2238	11.8890	321.0637	9.9533
	Figure 5C	5.6775	7.4494	384.6998	10.1785
	Figure 5D	4.9511	7.2061	128.4236	7.0026
	Figure 5E	6.2380	7.0719	275.0501	7.9808
	Figure 5F	6.0509	7.2392	398.1339	10.0982
	Figure 5G	7.2821	7.6919	165.2142	7.9315
	Figure 5H	6.0269	9.7018	385.3311	7.9389
	Figure 5I	7.0375	8.0875	250.3698	9.7501
	Figure 5J	6.1873	10.6472	334.8662	7.2176
Avg. (Std.)	6.8874 (2.0088)	8.5230 (1.6610)	279.2076 (102.7063)	8.2993 (1.7031)	

Bold indicates best result.

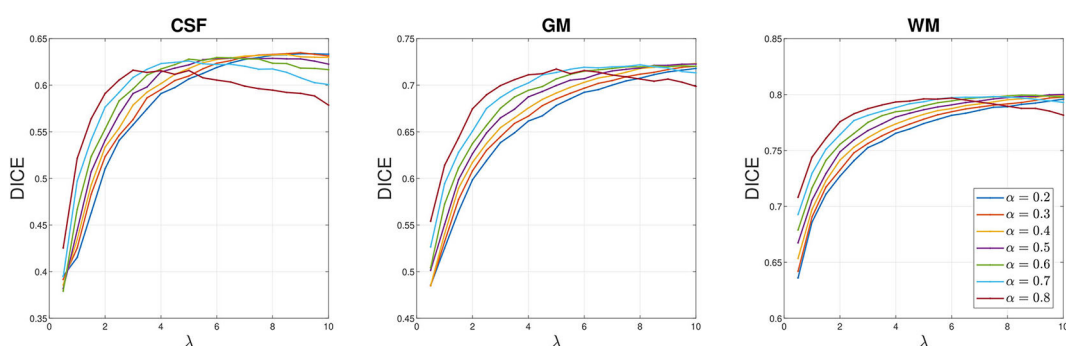


FIGURE 8

Sensitivity analysis on λ for the $P/8$ with motion blur case of Figure 3. The parameter $\mu = 1.0$ is fixed. DICE indices averaged over 20 images for each brain region are plotted with respect to λ .

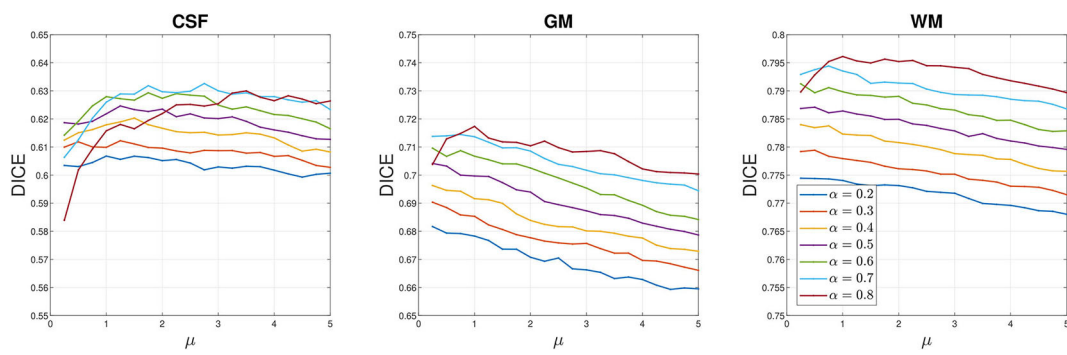


FIGURE 9

Sensitivity analysis on μ for the $P/8$ with motion blur case of Figure 3. The parameter $\lambda = 5.0$ is fixed. DICE indices averaged over 20 images for each brain region are plotted with respect to μ .

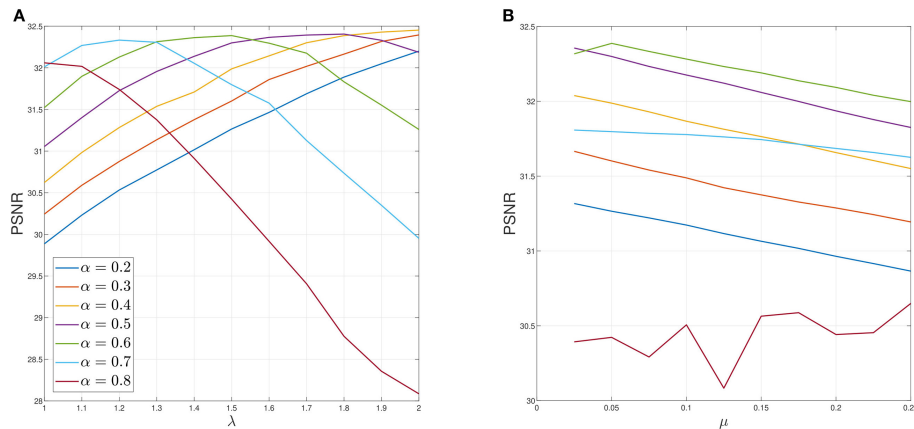


FIGURE 10

Sensitivity analysis of parameters for $P = 10$ case of Figure 5. (A) Sensitivity analysis on λ when $\mu = 0.05$ fixed. (B) Sensitivity analysis on μ when $\lambda = 1.5$ fixed. Average PSNR is plotted.

Zhang et al., 2022). Moreover, we plan to determine how to make the sparsity parameter α in AITV adaptable to each image. In future work, we will adapt other segmentation algorithms (Li et al., 2010, 2016; Jung et al., 2014; Jung, 2017; Cai et al., 2019; Yang et al., 2022; Pang et al., 2023) designed for Gaussian noise or impulsive noise to Poisson noise.

Data availability statement

Publicly available datasets were analyzed in this study. This data can be found at: <https://drive.grand-challenge.org/DRIVE/>; <https://github.com/casperdcl/brainweb>; <https://www2.eecs.berkeley.edu/Research/Projects/CS/vision/bsds/>. Code for AITV Poisson SaT/SLaT is available at https://github.com/kbui1993/Official_Poisson_AITV_SaT_SLaT.

Author contributions

KB performed the experiments and analysis and drafted the manuscript. All authors contributed to the design, evaluation, discussions, and production of the manuscript.

All authors contributed to the article and approved the submitted version.

Funding

This work was partially supported by NSF grants DMS-1846690, DMS-1854434, DMS-1952644, DMS-2151235, and a Qualcomm Faculty Award.

Conflict of interest

The authors declare that the research was conducted in the absence of any commercial or financial relationships that could be construed as a potential conflict of interest.

Publisher's note

All claims expressed in this article are solely those of the authors and do not necessarily represent those of their affiliated organizations, or those of the publisher, the editors and the reviewers. Any product that may be evaluated in this article, or claim that may be made by its manufacturer, is not guaranteed or endorsed by the publisher.

References

Ambrosio, L., and Tortorelli, V. M. (1990). Approximation of functional depending on jumps by elliptic functional via τ -convergence. *Commun. Pure Appl. Math.* 43, 999–1036. doi: 10.1002/cpa.3160430805

Anscombe, F. J. (1948). The transformation of Poisson, binomial and negative-binomial data. *Biometrika* 35, 246–254. doi: 10.1093/biomet/35.3-4.246

Aubert-Broche, B., Griffin, M., Pike, G. B., Evans, A. C., and Collins, D. L. (2006). Twenty new digital brain phantoms for creation of validation image data bases. *IEEE Trans. Med. Imaging* 25, 1410–1416. doi: 10.1109/TMI.2006.883453

Bar, L., Chan, T. F., Chung, G., Jung, M., Kiryati, N., Mohieddine, R., et al. (2011). “Mumford and Shah model and its applications to image segmentation and image restoration,” in *Handbook of Mathematical Methods in Imaging*, ed O. Scherzer (New York, NY: Springer), 1095–1157. doi: 10.1007/978-0-387-92920-0_25

Beck, A. (2017). *First-order Methods in Optimization*. Philadelphia, PA: SIAM. doi: 10.1137/1.9781611974997

Boyd, S., Parikh, N., Chu, E., Peleato, B., and Eckstein, J. (2011). Distributed optimization and statistical learning via the alternating direction method of multipliers. *Found. Trends Mach. Learn.* 3, 1–122. doi: 10.1561/22000000016

Bui, K., Fauman, J., Kes, D., Torres Mandiola, L., Ciomaga, A., Salazar, R., et al. (2020). Segmentation of scanning tunneling microscopy images using variational methods and empirical wavelets. *Pattern Anal. Appl.* 23, 625–651. doi: 10.1007/s10044-019-00824-0

Bui, K., Lou, Y., Park, F., and Xin, J. (2022). An efficient smoothing and thresholding image segmentation framework with weighted anisotropic-isotropic total variation. *arXiv preprint arXiv:2202.10115*. doi: 10.48550/arXiv.2202.10115

Bui, K., Park, F., Lou, Y., and Xin, J. (2021). A weighted difference of anisotropic and isotropic total variation for relaxed Mumford-Shah color and multiphase image segmentation. *SIAM J. Imaging Sci.* 14, 1078–1113. doi: 10.1137/20M1337041

Cai, X., Chan, R., Nikolova, M., and Zeng, T. (2017). A three-stage approach for segmenting degraded color images: smoothing, lifting and thresholding (SLaT). *J. Sci. Comput.* 72, 1313–1332. doi: 10.1007/s10915-017-0402-2

Cai, X., Chan, R., Schonlieb, C.-B., Steidl, G., and Zeng, T. (2019). Linkage between piecewise constant Mumford-Shah model and Rudin-Osher-Fatemi model and its virtue in image segmentation. *J. Sci. Comput.* 41, B1310–B1340. doi: 10.1137/18M1202980

Cai, X., Chan, R., and Zeng, T. (2013). A two-stage image segmentation method using a convex variant of the Mumford-Shah model and thresholding. *SIAM J. Imaging Sci.* 6, 368–390. doi: 10.1137/120867068

Cao, W., Sun, J., and Xu, Z. (2013). Fast image deconvolution using closed-form thresholding formulas of L_q ($q = \frac{1}{2}, \frac{2}{3}$) regularization. *J. Vis. Commun. Image Represent.* 24, 31–41. doi: 10.1016/j.jvcir.2012.10.006

Cascarano, P., Calatroni, L., and Piccolomini, E. L. (2021). Efficient ℓ^0 gradient-based super-resolution for simplified image segmentation. *IEEE Trans. Comput. Imaging* 7, 399–408. doi: 10.1109/TCI.2021.3070720

Chambolle, A., and Pock, T. (2011). A first-order primal-dual algorithm for convex problems with applications to imaging. *J. Math. Imaging Vis.* 40, 120–145. doi: 10.1007/s10851-010-0251-1

Chan, R., Yang, H., and Zeng, T. (2014). A two-stage image segmentation method for blurry images with Poisson or multiplicative Gamma noise. *SIAM J. Imaging Sci.* 7, 98–127. doi: 10.1137/130920241

Chan, T. F., Esedoglu, S., and Nikolova, M. (2006). Algorithms for finding global minimizers of image segmentation and denoising models. *SIAM J. Appl. Math.* 66, 1632–1648. doi: 10.1137/040615286

Chan, T. F., and Vese, L. A. (2001). Active contours without edges. *IEEE Trans. Image Process.* 10, 266–277. doi: 10.1109/83.902291

Chang, H., Lou, Y., Duan, Y., and Marchesini, S. (2018). Total variation-based phase retrieval for Poisson noise removal. *SIAM J. Imaging Sci.* 11, 24–55. doi: 10.1137/16M1103270

Chartrand, R. (2007). Exact reconstruction of sparse signals via nonconvex minimization. *IEEE Signal Process. Lett.* 14, 707–710. doi: 10.1109/LSP.2007.898300

Choksi, R., Gennip, Y. G., and Oberman, A. (2011). Anisotropic total variation regularized L^1 approximation and denoising/deblurring of 2D bar codes. *Inverse Probl. Imaging* 5, 591–617. doi: 10.3934/ipi.2011.5.591

Chowdhury, M. R., Qin, J., and Lou, Y. (2020a). Non-blind and blind deconvolution under Poisson noise using fractional-order total variation. *J. Math. Imaging Vis.* 62, 1238–1255. doi: 10.1007/s10851-020-00987-0

Chowdhury, M. R., Zhang, J., Qin, J., and Lou, Y. (2020b). Poisson image denoising based on fractional-order total variation. *Inverse Probl. Imaging* 14, 77–96. doi: 10.3934/ipi.2019064

Dice, L. R. (1945). Measures of the amount of ecological association between species. *Ecology* 26, 297–302. doi: 10.2307/1932409

Ding, L., and Han, W. (2019). $\alpha\ell_1 - \beta\ell_2$ regularization for sparse recovery. *Inverse Probl.* 35:125009. doi: 10.1088/1361-6420/ab34b5

Duan, Y., Chang, H., Huang, W., Zhou, J., Lu, Z., and Wu, C. (2015). The L_0 regularized Mumford-Shah model for bias correction and segmentation of medical images. *IEEE Trans. Image Process.* 24, 3927–3938. doi: 10.1109/TIP.2015.2451957

Evans, L. C. (2010). *Partial Differential Equations, Vol. 19*. Providence: American Mathematical Society. doi: 10.1090/gsm/019

Everingham, M., Van Gool, L., Williams, C. K., Winn, J., and Zisserman, A. (2009). The PASCAL visual object classes (VOC) challenge. *Int. J. Comput. Vis.* 88, 303–308. doi: 10.1007/s11263-009-0275-4

Ge, H., and Li, P. (2021). The Dantzig selector: recovery of signal via $\ell_1 - \alpha\ell_2$ minimization. *Inverse Probl.* 38:015006. doi: 10.1088/1361-6420/ac39f8

Gu, S., Xie, Q., Meng, D., Zuo, W., Feng, X., and Zhang, L. (2017). Weighted nuclear norm minimization and its applications to low level vision. *Int. J. Comput. Vis.* 121, 183–208. doi: 10.1007/s11263-016-0930-5

Guo, W., Lou, Y., Qin, J., and Yan, M. (2021). A novel regularization based on the error function for sparse recovery. *J. Sci. Comput.* 87, 1–22. doi: 10.1007/s10915-021-01443-w

Hintermüller, M., and Wu, T. (2013). Nonconvex TV^q -models in image restoration: analysis and a trust-region regularization-based superlinearly convergent solver. *SIAM J. Imaging Sci.* 6, 1385–1415. doi: 10.1137/110854746

Huo, L., Chen, W., Ge, H., and Ng, M. K. (2022). Stable image reconstruction using transformed total variation minimization. *SIAM J. Imaging Sci.* 15, 1104–1139. doi: 10.1137/21M1438566

Jung, M. (2017). Piecewise-smooth image segmentation models with l^1 data-fidelity terms. *J. Sci. Comput.* 70, 1229–1261. doi: 10.1007/s10915-016-0280-z

Jung, M., Kang, M., and Kang, M. (2014). Variational image segmentation models involving non-smooth data-fidelity terms. *J. Sci. Comput.* 59, 277–308. doi: 10.1007/s10915-013-9766-0

Lantéri, H., and Theys, C. (2005). Restoration of astrophysical images—the case of Poisson data with additive Gaussian noise. *EURASIP J. Adv. Signal Process.* 2005, 1–14. doi: 10.1155/ASP.2005.2500

Le, T., Chartrand, R., and Asaki, T. J. (2007). A variational approach to reconstructing images corrupted by Poisson noise. *J. Math. Imaging Vis.* 27, 257–263. doi: 10.1007/s10851-007-0652-y

Li, F., Ng, M. K., Zeng, T. Y., and Shen, C. (2010). A multiphase image segmentation method based on fuzzy region competition. *SIAM J. Imaging Sci.* 3, 277–299. doi: 10.1137/080736752

Li, F., Osher, S., Qin, J., and Yan, M. (2016). A multiphase image segmentation based on fuzzy membership functions and L1-norm fidelity. *J. Sci. Comput.* 69, 82–106. doi: 10.1007/s10915-016-0183-z

Li, H., Guo, W., Liu, J., Cui, L., and Xie, D. (2022). Image segmentation with adaptive spatial priors from joint registration. *SIAM J. Imaging Sci.* 15, 1314–1344. doi: 10.1137/21M1444874

Li, M.-M., and Li, B.-Z. (2022). A novel weighted anisotropic total variational model for image applications. *Signal Image Video Process.* 16, 211–218. doi: 10.1007/s11760-021-01977-4

Li, P., Chen, W., Ge, H., and Ng, M. K. (2020). $\ell_1 - \alpha\ell_2$ minimization methods for signal and image reconstruction with impulsive noise removal. *Inverse Probl.* 36:055009. doi: 10.1088/1361-6420/ab750c

Li, Y., Wu, C., and Duan, Y. (2020). The TV_p regularized Mumford-Shah model for image labeling and segmentation. *IEEE Trans. Image Process.* 29, 7061–7075. doi: 10.1109/TIP.2020.2997524

Liu, H., Deng, K., Liu, H., and Wen, Z. (2022). An entropy-regularized ADMM for binary quadratic programming. *J. Glob. Optim.* 1–33. doi: 10.1007/s10898-022-01144-0

Lou, Y., Osher, S., and Xin, J. (2015a). “Computational aspects of constrained $L_1 - L_2$ minimization for compressive sensing,” in *Modelling, Computation and Optimization in Information Systems and Management Sciences*, eds H. A. L. Thi, T. P. Dinh, and N. T. Nguyen (University of Lorraine, France: Springer), 169–180. doi: 10.1007/978-3-319-18161-5_15

Lou, Y., and Yan, M. (2018). Fast L1-L2 minimization via a proximal operator. *J. Sci. Comput.* 74, 767–785. doi: 10.1007/s10915-017-0463-2

Lou, Y., Yin, P., He, Q., and Xin, J. (2015b). Computing sparse representation in a highly coherent dictionary based on difference of L_1 and L_2 . *J. Sci. Comput.* 64, 178–196. doi: 10.1007/s10915-014-9930-1

Lou, Y., Zeng, T., Osher, S., and Xin, J. (2015c). A weighted difference of anisotropic and isotropic total variation model for image processing. *SIAM J. Imaging Sci.* 8, 1798–1823. doi: 10.1137/14098435X

Luong, Q.-T. (1993). "Color in computer vision" in *Handbook of Pattern Recognition and Computer Vision*, eds C. H. Chen, L. F. Pau, P. S. P. Wang (Singapore: World Scientific), 311–368. doi: 10.1142/9789814343138_0012

Mumford, D. B., and Shah, J. (1989). Optimal approximations by piecewise smooth functions and associated variational problems. *Commun. Pure Appl. Math.* 42, 577–685. doi: 10.1002/cpa.3160420503

Osher, S., and Sethian, J. A. (1988). Fronts propagating with curvature-dependent speed: algorithms based on Hamilton-Jacobi formulations. *J. Comput. Phys.* 79, 12–49. doi: 10.1016/0021-9991(88)90002-2

Pang, Z.-F., Geng, M., Zhang, L., Zhou, Y., Zeng, T., Zheng, L., et al. (2023). Adaptive weighted curvature-based active contour for ultrasonic and 3T/5T MR image segmentation. *Signal Process.* 205:108881. doi: 10.1016/j.sigpro.2022.108881

Park, F., Lou, Y., and Xin, J. (2016). "A weighted difference of anisotropic and isotropic total variation for relaxed Mumford-Shah image segmentation," in *2016 IEEE International Conference on Image Processing (ICIP)* (Phoenix, AZ), 4314–4318. doi: 10.1109/ICIP.2016.7533174

Pock, T., Chambolle, A., Cremers, D., and Bischof, H. (2009). "A convex relaxation approach for computing minimal partitions," in *2009 IEEE Conference on Computer Vision and Pattern Recognition* (Miami, FL), 810–817. doi: 10.1109/CVPR.2009.5206604

Potts, R. B. (1952). Some generalized order-disorder transformations. *Math. Proc. Cambrid. Philos. Soc.* 48, 106–109. doi: 10.1017/S0305004100027419

Rahimi, Y., Wang, C., Dong, H., and Lou, Y. (2019). A scale-invariant approach for sparse signal recovery. *SIAM J. Sci. Comput.* 41, A3649–A3672. doi: 10.1137/18M123147X

Rockafellar, R. T., and Wets, R. J.-B. (2009). *Variational Analysis*, Vol. 317. Berlin; Heidelberg: Springer Science & Business Media.

Rudin, L. I., Osher, S., and Fatemi, E. (1992). Nonlinear total variation based noise removal algorithms. *Phys. D* 60, 259–268. doi: 10.1016/0167-2789(92)90242-F

Staal, J., Abràmoff, M. D., Niemeijer, M., Viergever, M. A., and Van Ginneken, B. (2004). Ridge-based vessel segmentation in color images of the retina. *IEEE Trans. Med. Imaging* 23, 501–509. doi: 10.1109/TMI.2004.825627

Storath, M., and Weinmann, A. (2014). Fast partitioning of vector-valued images. *SIAM J. Imaging Sci.* 7, 1826–1852. doi: 10.1137/130950367

Storath, M., Weinmann, A., and Demaret, L. (2014). Jump-sparse and sparse recovery using Potts functionals. *IEEE Trans. Signal Process.* 62, 3654–3666. doi: 10.1109/TSP.2014.2329263

Tongbram, S., Shimray, B. A., Singh, L. S., and Dhanachandra, N. (2021). A novel image segmentation approach using FCM and whale optimization algorithm. *J. Ambient. Intell. Human. Comput.* 1–15. doi: 10.1007/s12652-020-02762-w

Vardi, Y., Shepp, L. A., and Kaufman, L. (1985). A statistical model for positron emission tomography. *J. Am. Stat. Assoc.* 80, 8–20. doi: 10.1080/01621459.1985.10477119

Vese, L. A., and Chan, T. F. (2002). A multiphase level set framework for image segmentation using the Mumford and Shah model. *Int. J. Comput. Vis.* 50, 271–293. doi: 10.1023/A:1020874308076

Wang, C., Tao, M., Chuah, C.-N., Nagy, J., and Lou, Y. (2022). Minimizing l_1 over l_2 norms on the gradient. *Inverse Probl.* 38:065011. doi: 10.1088/1361-6420/ac64fb

Wang, C., Tao, M., Nagy, J. G., and Lou, Y. (2021). Limited-angle CT reconstruction via the l_1/l_2 minimization. *SIAM J. Imaging Sci.* 14, 749–777. doi: 10.1137/20M1341490

Wang, C., Yan, M., Rahimi, Y., and Lou, Y. (2020). Accelerated schemes for the l_1/l_2 minimization. *IEEE Trans. Signal Process.* 68, 2660–2669. doi: 10.1109/TSP.2020.2985298

Wang, Y., Yang, J., Yin, W., and Zhang, Y. (2008). A new alternating minimization algorithm for total variation image reconstruction. *SIAM J. Imaging Sci.* 1, 248–272. doi: 10.1137/080724265

Wang, Y., Yin, W., and Zeng, J. (2019). Global convergence of ADMM in nonconvex nonsmooth optimization. *J. Sci. Comput.* 78, 29–63. doi: 10.1007/s10915-018-0757-z

Wen, Y., Chan, R. H., and Zeng, T. (2016). Primal-dual algorithms for total variation based image restoration under Poisson noise. *Sci. China Math.* 59, 141–160. doi: 10.1007/s11425-015-5079-0

Wu, T., Gu, X., Wang, Y., and Zeng, T. (2021a). Adaptive total variation based image segmentation with semi-proximal alternating minimization. *Signal Process.* 183:108017. doi: 10.1016/j.sigpro.2021.108017

Wu, T., Mao, Z., Li, Z., Zeng, Y., and Zeng, T. (2022a). Efficient color image segmentation via quaternion-based L_1/L_2 regularization. *J. Sci. Comput.* 93:9. doi: 10.1007/s10915-022-01970-0

Wu, T., Shao, J., Gu, X., Ng, M. K., and Zeng, T. (2021b). Two-stage image segmentation based on nonconvex $\ell_2 - \ell_p$ approximation and thresholding. *Appl. Math. Comput.* 403:126168. doi: 10.1016/j.amc.2021.126168

Wu, T., Zhao, Y., Mao, Z., Shi, L., Li, Z., and Zeng, Y. (2022b). Image segmentation via Fischer-Burmeister total variation and thresholding. *Adv. Appl. Math. Mech.* 14, 960–988. doi: 10.4208/aamm.OA-2021-0126

Xu, Y., Narayan, A., Tran, H., and Webster, C. G. (2021). Analysis of the ratio of l_1 and l_2 norms in compressed sensing. *Appl. Comput. Harmon. Anal.* 55, 486–511. doi: 10.1016/j.acha.2021.06.006

Xu, Y., Yin, W., Wen, Z., and Zhang, Y. (2012). An alternating direction algorithm for matrix completion with nonnegative factors. *Front. Math. China* 7, 365–384. doi: 10.1007/s11464-012-0194-5

Xu, Z., Chang, X., Xu, F., and Zhang, H. (2012). $L_1/2$ regularization: a thresholding representation theory and a fast solver. *IEEE Trans. Neural Netw. Learn. Syst.* 23, 1013–1027. doi: 10.1109/TNNLS.2012.2197412

Yang, J., Guo, Z., Zhang, D., Wu, B., and Du, S. (2022). An anisotropic diffusion system with nonlinear time-delay structure tensor for image enhancement and segmentation. *Comput. Math. Appl.* 107, 29–44. doi: 10.1016/j.camwa.2021.12.005

You, J., Jiao, Y., Lu, X., and Zeng, T. (2019). A nonconvex model with minimax concave penalty for image restoration. *J. Sci. Comput.* 78, 1063–1086. doi: 10.1007/s10915-018-0801-z

Zhang, T., Chen, J., Wu, C., He, Z., Zeng, T., and Jin, Q. (2022). Edge adaptive hybrid regularization model for image deblurring. *Inverse Probl.* 38:065010. doi: 10.1088/1361-6420/ac60bf

Zosso, D., An, J., Stevick, J., Takaki, N., Weiss, M., Slaughter, L. S., et al. (2017). Image segmentation with dynamic artifacts detection and bias correction. *Inverse Probl. Imaging* 11, 577–600. doi: 10.3934/ipi.2017027